

1 Coastal Atmosphere & Sea Time Series (CoASTS) and Bio-Optical mapping of
2 Marine optical Properties (BiOMaP): the CoASTS-BiOMaP dataset.

3

4

Giuseppe Zibordi¹ and Jean-François Berthon²

5

6 | ¹*National Aeronautics and Space Administration, Goddard Space Flight Center, [Greenbelt](#), MD USA*

7

²*Joint Research Centre of the European Commission, Ispra, Italy*

8

9

Correspondence to: Giuseppe Zibordi (giuseppe.zibordi@eoscience.eu)

ABSTRACT

The *Coastal Atmosphere & Sea Time Series* (CoASTS) and the *Bio-Optical mapping of Marine optical Properties* (BiOMaP) programs produced bio-optical data supporting satellite ocean color applications for more than two decades. Specifically, relying on the Acqua Alta Oceanographic Tower (AAOT) in the northern Adriatic Sea, from 1995 till 2016 CoASTS delivered time series of marine water apparent and inherent optical properties, in addition to the concentration of major optically significant water constituents. Almost concurrently, from 2000 till 2022 BiOMaP produced equivalent spatially distributed measurements across major European Seas. Both, CoASTS and BiOMaP applied ~~equal~~-standardized instruments, measurement methods, quality control schemes and processing codes to ensure temporal and spatial consistency to data products. This work presents the CoASTS and BiOMaP near surface data products, named CoASTS-BiOMaP, of relevance for ocean color bio-optical modelling and validation activities.

1. Introduction

The validation of primary (*i.e.*, radiometric) and derived (*e.g.*, phytoplankton pigments concentration) satellite data products, as well as the development of bio-optical algorithms linking radiometric data to the inherent optical properties or to the concentration of natural water optically significant constituents, require accurate and comprehensive *in situ* bio-optical measurements (*e.g.*, see Werdell and Bailey 2007). Anticipating this need for the Sea-Wide Field-of-View (SeaWiFS) ocean color mission, during the 90s several measurement programs were established to gather bio-optical data representative of the world marine waters. Among these, the *Coastal Atmosphere & Sea Time Series* (CoASTS) and the *Bio-Optical mapping of Marine optical Properties* (BiOMaP) measurement programs implemented by the Marine Optical Laboratory (Belward et al. 2022) of the Joint Research Center (JRC) in collaboration with a number of European institutions, produced comprehensive *in situ* bio-optical measurements of relevance for satellite ocean color applications. While CoASTS benefited of the Acqua Alta Oceanographic Tower (AAOT) in the northern Adriatic Sea to generate time-series data at a fixed coastal site (Berthon et al. 2002; Zibordi et al. 2002), BiOMaP relied on oceanographic ships to collect spatially distributed measurements across various European Seas (Berthon et al. 2008, Zibordi et al. 2011). Both CoASTS and BiOMaP endorsed standardization of instruments, measurement methods, quality control schemes and processing codes to enforce consistency to temporally and spatially distributed data products. It is still recognized that some of the measurement methods primarily implemented for optically complex coastal waters, may not warrant the desirable high accuracy in oligotrophic clear waters.

Overall, CoASTS and BiOMaP data extend over a period exceeding two decades and constitute a unique dataset for bio-optical investigations across a variety of water types with potential application to climate change studies.

Objective of this work is to introduce the CoASTS and BiOMaP derived data products relevant for satellite ocean color applications. Specifically, the near-surface data products with spectral values restricted to key ocean colour center-wavelengths; are presented together with a description of the measurement and data reduction methods.

2. The CoASTS and BiOMaP programs

CoASTS and BiOMaP were conceived as complementary programs: CoASTS focused on the generation of time-series of reference data from a fixed coastal site showing significant seasonal cycles and moderately bio-optical complexity (Berthon et al. 2002); conversely BiOMaP covered a variety of marine regions exhibiting very diverse bio-optical regimes, but with limited temporal representativity (Berthon et al. 2008).

The use of an oceanographic tower as logistic platform for comprehensive optical and bio-geochemical measurements, when compared to oceanographic ships, does not allow for spatially extended observations. However, it offers the unique opportunity of a very stable measurement platform enabling easy control of the deployment geometry of optical instruments with respect to the structure. Specifically, regardless of sea state, the use of the AAOT as measurement platform made possible deploying optical sensors relying on tower–sensor–Sun geometry favouring the application of corrections for the minimization of potential superstructure perturbations in radiometric data (Zibordi et al. 1999, Doyle and Zibordi 2002).

CoASTS measurements are representative of marine frontal regions exhibiting occurrence of waters with optical properties largely determined by phytoplankton and its degradation components (*i.e.*, Case 1 waters), as wells as optically complex waters characterized

72 | by moderate concentrations of sediments and coloured organic matter (CDOM), with bio-optical
73 | variability determined by the impact of local currents, seasonal changes in biological regimes
74 | and rivers discharge (Berthon et al. 2002).

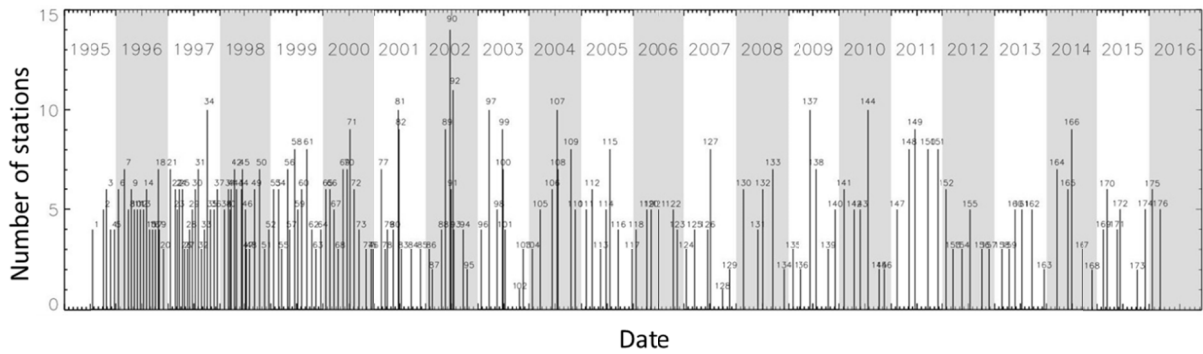
75 | CoASTS measurements took place with monthly occurrence since 1995. However, from
76 | 2001 and up to the end of the measurement program in 2016, the frequency of field
77 | measurements was reduced to one every 2-3 months. Each comprehensive data collection —
78 | called a *station* — included in-water optical and hydrographic profiles, seawater samples at
79 | different depths (*i.e.*, near surface, 8 m and 14 m), meteorological data, and visual observations
80 | of cloud cover and sea state. CoASTS comprises 176 field campaigns leading to 883
81 | measurement stations. Still, only CoASTS campaigns and stations performed from December
82 | 1998 onward (*i.e.*, 125 and 617, respectively) fulfil the requirement of measurements
83 | standardization.

84 | Spatially distributed measurements are best possible using oceanographic ships. Because
85 | of this, BiOMaP measurements were performed relying on research vessels across a variety of
86 | bio-optical regions (see Berthon et al. 2008): the Baltic Sea exhibiting waters dominated by a
87 | high concentration of CDOM; the Adriatic Sea, Black Sea, North Sea (including the English
88 | Channel), Ligurian Sea, Iberian Shelf and the Greenland Sea, characterized by a variety of
89 | optically complex waters determined by diverse concentrations of CDOM and suspended
90 | particulate matter (SPM); the Eastern and Western Mediterranean oligotrophic and mesotrophic
91 | Seas with optical properties largely determined by phytoplankton and its degradation
92 | components.

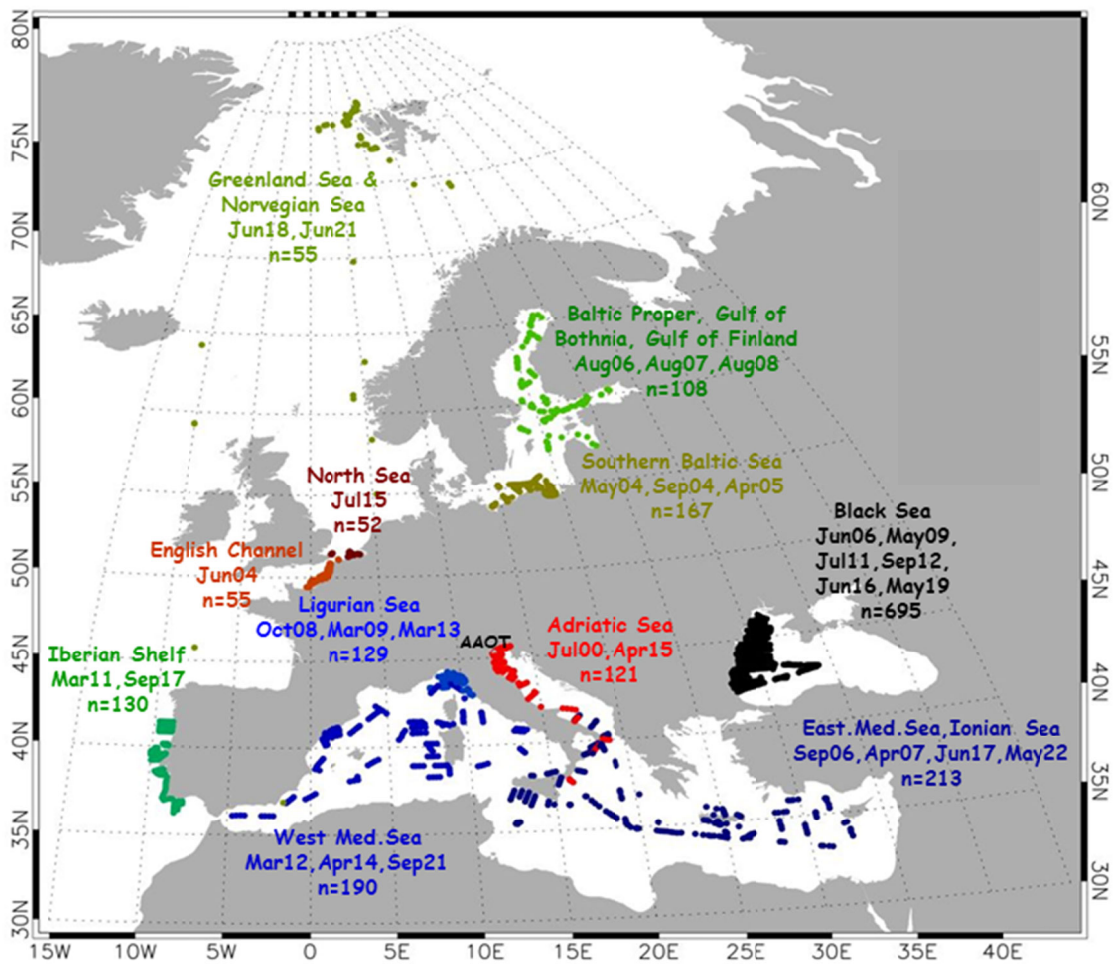
93 | BiOMaP, encompassing 36 bio-optical oceanographic campaigns and 1915 measurement
94 | stations, started in 2000 and ended in 2022. It is mentioned that some measurements from 33
95 | BiOMaP stations performed in the Black Sea during 2011 were included in an independent
96 | dataset constructed to support the validation of satellite data products (Valente et al. 2016).

97 | As already anticipated, measurement consistency between the CoASTS and BiOMaP
98 | programs was achieved using identical field and laboratory instrumentation, and applying the
99 | same consolidated methods, quality control schemes and processing codes.— Consequently,
100 | BiOMaP measurements performed during each station exhibit equivalence with those of
101 | CoASTS, except for restricting the collection of water samples to the near surface. Finally,
102 | superstructure perturbations in BioMaP radiometric data were avoided by operating optical
103 | radiometers on free-fall profilers deployed at some distance from ships (IOCCG 2019).

104 |
105 | Figure 1 shows the temporal evolution of CoASTS measurement campaigns and the number
106 | of stations per campaign. These latter were largely benefitting of sea state conditions allowing
107 | access to the tower. Figure 2 shows the overall distribution of BiOMaP stations across the
108 | various European Seas.



111
 112 Figure 1. CoASTS measurement campaigns (176 total, 125 since December 1998) and stations
 113 | (883 total, ~~617-637~~ since December 1998) completed between 1995 and 2016.
 114



115

116

117 Figure 2. BiOMaP oceanographic campaigns (36) and measurement stations (1915) performed
 118 | between 2000 and 2022.

119

120 Table 1. The CoASTS measurement program: campaign identifiers, marine region, years,
 121 number of stations, research platform, collaborating institution.

122

Campaign ID	Location	Year	Stations #	Research platform	Collaborating Institution
V03-V99	Northern Adriatic Sea (AAOT)	1998-2011	481	<i>Acqua Alta Oceanog. Tower (AAOT)</i>	Italian National Research Council (IT)
W01-W28	Northern Adriatic Sea (AAOT)	2011-2016	136	<i>Acqua Alta Oceanog. Tower (AAOT)</i>	Italian National Research Council (IT)

123

124

125

126 Table 2. The BiOMaP measurement program: campaign identifiers, marine regions, year,
 127 number of stations, research vessels, collaborating institutions.

128

Campaign ID	Region	Year	Stations #	Research vessel	Collaborating Institution
A01	Adriatic Sea (ADRS)	2000	55	<i>R/V Friuli-Venezia Giulia (FVG)</i>	University of Trieste (IT)
A02	Adriatic Sea (ADRS)	2014	66	<i>R/V Minerva-1</i>	Italian National Research Council (IT)
B01	Baltic Sea (BLTS)	2004	52	<i>R/V Oceania</i>	Institute of Oceanology (PL)
B02	Baltic Sea (BLTS)	2004	52	<i>R/V Oceania</i>	Institute of Oceanology (PL)
B03	Baltic Sea (BLTS)	2005	63	<i>R/V Oceania</i>	Institute of Oceanology (PL)
B04	Baltic Sea (BLTS)	2006	23	<i>R/V Aranda</i>	Institute of Marine Research (FI)
B05	Baltic Sea (BLTS)	2007	38	<i>R/V Aranda</i>	Institute of Marine Research (FI)
B06	Baltic Sea (BLTS)	2008	47	<i>R/V Aranda</i>	Institute of Marine Research (FI)
E01	Eastern Med. Sea (EMED)	2006	62	<i>R/V Urania</i>	Italian National Research Council (IT)
E02	Eastern Med. Sea (EMED)	2007	69	<i>R/V Urania</i>	Italian National Research Council (IT)
E03	Eastern Med. Sea (EMED)	2017	51	<i>R/V Minerva-1</i>	Italian National Research Council (IT)
E04	Eastern Med. Sea (EMED)	2022	31	<i>R/V Philia</i>	Hellenic Centre for Marine Research (GR)
I01	Iberian Shelf (IBSH)	2011	68	<i>NRP Almirante Gago Coutinho</i>	Portuguese Hydrographic Institute (PT)
I02	Iberian Shelf (IBSH)	2017	62	<i>NRP Almirante Gago Coutinho</i>	Portuguese Hydrographic Institute (PT)
K01	Black Sea (BLKS)	2006	93	<i>R/V Akademik</i>	Institute of Oceanology (BG)
K02	Black Sea (BLKS)	2009	73	<i>R/V Akademik</i>	Institute of Oceanology (BG)
K03	Black Sea (BLKS)	2009	40	<i>R/V Akademik</i>	Institute of Oceanology (BG)

K04	Black Sea (BLKS)	2011	38	<i>R/V Mare Nigrum</i>	National Institute of Marine Geology and Geoecology (RO)
K05	Black Sea (BLKS)	2011	24	<i>R/V Akademik</i>	Institute of Oceanology (BG)
K06	Black Sea (BLKS)	2011	59	<i>R/V Akademik</i>	Institute of Oceanology (BG)
K07	Black Sea (BLKS)	2012	93	<i>R/V Akademik</i>	Institute of Oceanology (BG)
K08	Black Sea (BLKS)	2012	14	<i>R/V Akademik</i>	Institute of Oceanology (BG)
K09	Black Sea (BLKS)	2016	54	<i>R/V Akademik</i>	Institute of Oceanology (BG)
K10	Black Sea (BLKS)	2016	83	<i>R/V Akademik</i>	Institute of Oceanology (BG)
K11	Black Sea (BLKS)	2019	80	<i>R/V Akademik</i>	Institute of Oceanology (BG)
K12	Black Sea (BLKS)	2019	44	<i>R/V Akademik</i>	Institute of Oceanology (BG)
L01	Ligurian Sea (LIGS)	2008	41	<i>R/V Alliance</i>	Undersea Research Center (NATO)
L02	Ligurian Sea (LIGS)	2009	63	<i>R/V Alliance</i>	Undersea Research Center (NATO)
L04	Ligurian Sea (LIGS)	2013	25	<i>R/V Alliance</i>	Undersea Research Center (NATO)
N01	English Channel & North Sea (NORS)	2004	55	<i>R/V Côtes de la Manche</i>	Université du Littoral Côte d'Opale (FR)
N02	North Sea (NORS)	2015	52	<i>R/V Belgica</i>	Royal Belgian Institute of Natural Sciences (BE)
O01	Western Med. Sea (WMED)	2012	73	<i>R/V Urania</i>	Italian National Research Council (IT)
O02	Western Med. Sea (WMED)	2014	64	<i>R/V Urania</i>	Italian National Research Council (IT)
O03	Western Med. Sea (WMED)	2021	53	<i>R/V Garcia del Cid</i>	Institute of Marine Science (ES)
P01	Greenland Sea (GRLS)	2018	15	<i>R/V Alliance</i>	Undersea Research Center (NATO)
P03	Greenland Sea ¹ (GRLS)	2021	40	<i>R/V Alliance</i>	Italian Hydrographic Institute (IT)

¹ It includes stations from the Norwegian Sea.

129
130
131
132
133
134
135
136
137
138
139
140

3. **Measurements overview**

CoASTS and BiOMaP core data comprise *in situ* and laboratory measurements performed on samples prepared in the field. The firsts include:

- a. **Multispectral** profiles of upwelling nadir radiance $L_u(z, \lambda)$, downward irradiance $E_d(z, \lambda)$, and upward irradiance $E_u(z, \lambda)$, where z indicates **the** depth and λ the center-wavelength of each spectral band;
- b. **Multispectral above-water** downward irradiance $E_s(t, \lambda)$ **acquired during in-water profiling (where t is the time corresponding to the depth z)** and diffuse sky irradiance $E_i(t, \lambda)$ **acquired at the end of each station with an irradiance sensor operated in conjunction with a rotating shadow band;**

- 141 c. Multispectral profiles of beam attenuation $c(z,\lambda)$, absorption $a(z,\lambda)$ and backscattering
 142 | $b_b(z,\lambda)$ coefficients, commonly restricted to the first 25 m depth for BiOMaP and 15 m
 143 for CoASTS;
 144 d. Profiles of water temperature $T_w(z)$ and salinity $S_w(z)$, also restricted to the first 25 m
 145 depth for BiOMaP and 15 m for CoASTS;
 146 e. Meteorological data including wind speed W_s in addition to cloud cover C_c and sea state
 147 S_s observations.

148 | The laboratory measurements performed on field samples, complementary to [the *in situ* ones](#),
 149 are:

- 150 | f. Spectral *in vivo* particulate absorption coefficients $a_{ph}(\lambda)$ for the pigmented and- [a_{dit}\(λ\)](#) for
 151 the non-pigmented particles;
 152 g. Spectral CDOM absorption coefficient $a_{ys}(\lambda)$;
 153 h. Phytoplankton pigments concentration;
 154 | i. [Suspended particulate matter concentration SPM](#).

156 | 4. Measurements and data reduction methods

157 Information on measurement methods and data reduction are summarized in the following
 158 subsections.

160 | 4.1 Radiometric products

161 CoASTS in-water radiometric measurements of $L_u(z,\lambda)$, $E_d(z,\lambda)$, $E_u(z,\lambda)$ were performed
 162 with the Wire-Stabilized Profiling Environmental Radiometer (WiSPER) using Satlantic
 163 (Halifax, Canada) OCR/OCI-200 multispectral radiometer series. Concurrently, [above-water](#)
 164 $E_s(t,\lambda)$ and $E_i(t,\lambda)$ measurements were also [collected](#) with OCI-200 radiometers. In the case of
 165 BiOMaP, the equivalent measurements were performed using miniPRO and microPRO Satlantic
 166 custom designed free-fall profilers equipped with OCR/OCI-200 or alternatively OCR-507
 167 multispectral radiometers. All radiometric quantities were measured with 6 Hz acquisition rate [at](#)
 168 | spectral bands relevant for ocean color applications [with](#) 10 nm bandwidth and nominal center-
 169 wavelenghts at 412, 443, 490, 510, 555, 665 and 683 nm. WiSPER data were gathered with a
 170 deployment speed of 0.1 m s⁻¹. Conversely, the deployment speed of the free-fall systems
 171 generally varied in the range of approximately 0.3-0.4 m s⁻¹. The collection of in-water
 172 radiometric measurements with low tilt and as close as possible to the surface, was always
 173 attempted to ensure best retrieval of subsurface radiometric values through the extrapolation of
 174 profile data.

175 The regular absolute radiometric calibration of field optical radiometers was performed at
 176 the JRC Marine Optical Laboratory using 1000W FEL lamps traceable to the National Institute
 177 of Standards and Technology (NIST) or alternatively the National Physical Laboratory (NPL).
 178 While CoASTS radiometers were re-calibrated on a six-monthly basis, BiOMaP radiometers
 179 were calibrated before and after each oceanographic campaign. Regular inter-calibrations
 180 between the JRC Marine Optical Laboratory and the National Aeronautics and Space
 181 Administration (NASA) performed within the framework of the Ocean Color component of the
 182 Aerosol Robotic Network (AERONET-OC), ensured continuous verification of the accuracy of
 183 the calibration process (Zibordi et al. 2021).

184 Data pre-processing included: *i.* the application of absolute calibration coefficients and
 185 immersion factors for in-water radiometers (Zibordi et al. 2004; Zibordi 2006); *ii.* the removal of
 186 | in-water and [in-air](#) data exhibiting tilt higher than 5° (this was confidently established from 2009

187 for BiOMaP $E_s(t, \lambda)$ and $E_i(t, \lambda)$); *iii.* limited to BiOMaP, the composition of successive profile
188 data typically collected within a 5 min interval to create multi-cast **combined** profiles to increase
189 the number of measurements per unit depth and consequently improve the **precision** of
190 extrapolated values; and *iv.* the correction of in-air irradiance data for the non-cosine response of
191 collectors (see Zibordi and Bulgarelli 2007). **Additional corrections for sensors non-ideal
192 performance, such as out-of-band response or temperature dependence, were not implemented
193 being considered minor for the multispectral instruments applied.**

194 In agreement with consolidated protocols (*e.g.*, see IOCCG 2019), the **impact** of **illumination
195 changes in profile data** were minimized through normalization of each radiometric quantity with
196 respect to above-water downward irradiance $E_s(t, \lambda)$ simultaneous to the in-water **measurements**.
197 Specifically, the normalization aimed at producing radiometric quantities as if they were taken at
198 the same time t_0 at each depth z , where t_0 was chosen to coincide with the beginning of the
199 acquisition sequence during each cast or multi-cast.

200 The sub-surface quantities $L_u(0^-, \lambda)$, $E_u(0^-, \lambda)$ and $E_d(0^-, \lambda)$ were then determined at the
201 depth $z_0 = 0$ (identified by 0^-) as the exponentials of the intercepts resulting from the least-
202 squares linear regressions of $\ln \mathfrak{I}(z, \lambda)$ versus z within the extrapolation interval $z_0 - z_1$, where
203 $\mathfrak{I}(z, \lambda)$ indicates either $L_u(z, \lambda)$, $E_d(z, \lambda)$ or $E_u(z, \lambda)$ normalized with respect to $E_s(t, \lambda)$ at matching
204 times. The extrapolation interval **was** chosen on a profile-by-profile basis with the aid of
205 absorption and scattering profile data to identify **the depths z_0 and z_1 , generally comprised within
206 0.3 and 5 m and** best satisfying the requirement of linear decay with depth of the log-transformed
207 radiometric **values**. **It is pointed out that the application of linear extrapolations to log-
208 transformed data to determine sub-surface radiometric values, alternative to use of non-linear
209 exponential extrapolations (see D’Alimonte et al 2012), was suggested by the objective to ensure
210 consistency with existing radiometric data datasets.**

211 **Extreme outliers** in the $z_0 - z_1$ depth interval generally due to **major** wave focusing **and
212 shadowing effects**, were excluded from the extrapolation process by removing points exhibiting
213 distance higher than 3σ from the linear regression line, where σ is the standard deviation of the
214 differences between data points and regression line. **This filtering process is mostly effective in
215 the presence of a relatively small number of points in the extrapolation layer. The application of
216 a very slow deployment speed in the case of CoASTS radiometric data and the application of the
217 multi-cast method for BiOMaP data, ensured the availability of hundreds of measurements in
218 each selected extrapolation interval. This restricts the application of the 3σ filter to a few
219 extreme values without significantly impacting the precision of the extrapolated data.**

220 The $L_u(0^-, \lambda)$ and $E_u(0^-, \lambda)$ data products were corrected for self-shading and potential
221 bottom perturbations (Zibordi et al. 2002). Additionally, limited to CoASTS data collected in
222 the vicinity of the AAOT, corrections were **also** applied for perturbations due to the deployment
223 structure (Doyle and Zibordi 2002, Doyle et al. 2003). BiOMaP data, generally collected at
224 distances from the ship of approximately 15–30 m, did not require corrections for the
225 perturbations by the **deployment** structure.

226 In addition to $L_u(0^-, \lambda)$, $E_u(0^-, \lambda)$ and $E_d(0^-, \lambda)$, further retrieved data products are the
227 slopes of the regression fits $K_{\mathfrak{I}}(\lambda)$ (*i.e.*, $K_{L_u}(\lambda)$, $K_{E_u}(\lambda)$ and $K_d(\lambda)$) in the extrapolation interval,
228 *i.e.*, the diffuse attenuation coefficients. **These $K_{\mathfrak{I}}(\lambda)$ values and particularly $K_d(\lambda)$, may exhibit
229 underestimated values due to the impact of wave focussing in the near surface water layer. This
230 effect is expected to be more pronounced for radiometric profiles collected in clear waters during
231 clear sky conditions.**

232 **Derived radiometric data products are then the remote sensing reflectance $R_{rs}(\lambda)$**

233
234 |
$$R_{rs}(\lambda) = L_w(\lambda)/E_s(\lambda) \quad (1)$$

235
236 and the normalized water-leaving radiance $L_{wn}(\lambda)$

237
238 |
$$L_{wn}(\lambda) = R_{rs}(\lambda)E_0(\lambda), \quad (2)$$

239
240 | where $E_s(\lambda)$ refers to the value measured at time t_0 , $E_0(\lambda)$ is the extra-atmospheric solar
241 irradiance (Thuillier et al. 2003) at the mean sun-earth distance, and $L_w(\lambda)$ is the water-leaving
242 radiance, *i.e.*, the radiance leaving the sea and quantified just above the surface through the
243 extrapolation process, given by

244
245 |
$$L_w(\lambda) = 0.544 L_u(0^-, \lambda). \quad (3)$$

246
247 where the factor 0.544 accounts for the radiance reduction across the water surface due to the
248 change in the refractive index at the air-water interface, as determined assuming that the
249 refractive index of seawater is independent of wavelength (Austin 1974). It is acknowledged that
250 the values of $L_w(\lambda)$ determined with Eq. 3 exhibit differences well within $\pm 1\%$ with respect to
251 the values computed accounting for the spectral dependence of the water refractive index in the
252 spectral range of interest (Voss and Flora 2017).

253 Finally, supplementary derived quantity is the Q -factor at nadir $Q_n(0^-, \lambda)$ determined by the
254 ratio of $E_u(0^-, \lambda)$ to $L_u(0^-, \lambda)$ spectrally fitted to a quadratic function in the 412-555 nm spectral
255 interval to minimize the impact of calibration and extrapolation uncertainties. The ratio of fitted
256 $Q_n(0^-, \lambda)$ to $E_u(0^-, \lambda) / L_u(0^-, \lambda)$ provides a basic approach to evaluate the relative consistency
257 of the $E_u(0^-, \lambda)$ and $L_u(0^-, \lambda)$ multispectral values (*e.g.*, any appreciable bias affecting a single
258 spectral value leads to a spectral inconsistency in $E_u(0^-, \lambda) / L_u(0^-, \lambda)$).

259 The quantities $R_{rs}(\lambda)$ and $L_{wn}(\lambda)$, due to the normalization with respect to $E_s(\lambda)$, benefit of a
260 first correction for changes in illumination conditions with sun zenith, sun-earth distance and
261 atmospheric transmittance (Mueller and Austin 1995).– The additional correction performed
262 through the application of the $C_{f/Q}(\theta_0, \lambda, \tau_a, IOP)$ factors to $L_{wn}(\lambda)$ and analogously to $R_{rs}(\lambda)$,
263 accounts for in-water bi-directional effects, and leads to the determination of the final $L_{WN}(\lambda)$ and
264 $R_{RS}(\lambda)$ data products. The $C_{f/Q}$ factors are a function of the water inherent optical properties IOP
265 (absorption and back-scattering coefficients), the atmospheric optical properties conveniently
266 expressed through the aerosol optical depth τ_a and the sun zenith angle θ_0 . These correction
267 factors were determined applying the tabulated values proposed by Morel et al. (2002) for Case 1
268 waters with $IOPs$ solely expressed as a function of total chlorophyll-*a* concentration ($-Chla$) as
269 determined from water samples for each measurement station. It is acknowledged that this
270 correction may be affected by large uncertainties when applied to optically complex waters. Still,
271 the inclusion of both $L_w(\lambda)$ and $E_s(\lambda)$, as well as spectral values of the water inherent optical
272 properties, would allow any potential user of the CoASTS-BiOMaP data set to implement
273 alternative solutions for the determination of $L_{WN}(\lambda)$ and $R_{RS}(\lambda)$.

274 An estimate of the uncertainties for CoASTS and BiOMaP L_{WN} and similarly R_{RS} data, was
275 attempted and discussed in various publications (Zibordi and Voss 2010, Zibordi et al. 2011)
276 accounting for the major uncertainties characterizing: *i.* absolute calibration coefficients and
277 immersion factors; *ii.* correction factors for shading perturbations; *iii.* correction factors for in-
278 water bidirectional effects; *iv.* the determination of $E_s(\lambda)$; *v.* the quantification of $E_0(\lambda)$ when

279 ignoring actual bandwidths; *vi.* the extrapolation process for the computation of sub-surface data;
280 and *vii.* finally, environmental stability as a result of wave perturbations and changes in
281 illumination conditions and seawater optical properties during profiling. In the specific case of
282 moderately optically complex waters such as those characterizing CoASTS measurements, the
283 uncertainties affecting L_{WN} and R_{RS} are expected to approach 5% in the blue green spectral
284 region and 7% in the red. In agreement with analyses performed for alternative *in situ*
285 radiometric methods (Gergely and Zibordi 2014), the above relative uncertainties may become
286 significantly larger in the blue spectral region for data products from marine regions
287 characterized by high water absorption such as the Baltic Sea.

288 Quality indices for radiometric products were determined during data processing in view
289 of supporting an evaluation of their accuracy. These include: *i.* the ratio $Q_R(412) = Q_n(0^-, 412) /$
290 $Q_n(1, 412)$ of Q_n - values determined at 0⁻ and 1 m depths at the 412 nm center-wavelength,
291 whose significant deviation from 1 suggests issues in the extrapolation of sub-surface values; *ii.*
292 the coefficient of variation $CV_{E_s(412)}$ of in-air downward irradiance for the extrapolation
293 interval, whose high value indicates significant perturbations by ship movement or changes in
294 illumination conditions during profiling; *iii.* the diffuse to direct ratio of above-water downward
295 irradiance $R_d(412)$, whose high values indicates poor illumination conditions likely due to high
296 sun zeniths or cloudiness; *iv.* the index $R_i(412) = E_s(412) / [1.04 E_d(412)]$, whose significant
297 deviation from 1 indicates inconsistency between in-air and in-water measurements of the
298 downward irradiance; and finally v. the index $K_i(490)$ determined by the difference between
299 $K_d(490)$ and the corresponding value for pure water $K_w(490)$ set to 0.0212 m^{-1} (Smith and
300 Baker 1981), whose negative value identifies radiometric data products (mostly related to clear
301 waters and clear sky conditions) significantly challenged by wave perturbations.

302

303 4.2 Absorption and attenuation from profile data

304 Beam attenuation $c_{t-w}(z, \lambda)$ and absorption $a_{t-w}(z, \lambda)$ coefficients, excluding the contribution of
305 pure seawater, were determined from measurements performed using AC9s instruments from
306 WET Labs Inc. (Philomath, Oregon) with 25 cm path-length and nine spectral bands 10 nm wide
307 at the 412, 440, 488, 510, 555, 630, 650, 676 and 715 nm center-wavelengths. The values of
308 $c_{t-w}(z, \lambda)$ and $a_{t-w}(z, \lambda)$, in agreement with the scheme proposed by the instrument manufacturer
309 (WET Labs 2006-), were corrected for the effects of differences in temperature T_w and salinity S_w
310 between field measurements and laboratory calibrations. These corrections were performed using
311 $T_w(z)$ and $S_w(z)$ profile data simultaneously to the AC9 ones.

312 AC9 absorption coefficients need correction for ~~the finite acceptance angle of the detector~~
313 ~~and~~ the non-completely reflective surfaces of the absorption measurement tube, which prevents
314 the collection of the whole scattered light and naturally leads to an overestimate of $a_{t-w}(z, \lambda)$. This
315 corrections was performed by removing a variable percentage of the scattering coefficient b_{t-}
316 $w(z, \lambda)$ estimated from the difference between $c_{t-w}(z, \lambda)$ and $a_{t-w}(z, \lambda)$ at each λ , assuming the
317 absorption coefficient of particulate and dissolved material is zero at the reference wavelength λ_0
318 = 715 nm and the shape of the volume scattering function is spectrally independent (Zaneveld et
319 al. 1992). Recent investigations showed this correction method may lead to significant
320 underestimates of $a_{t-w}(z, \lambda)$. Still, it was used in the CoASTS-BiOMaP data processing because
321 alternative promising correction methods such as that proposed by Roettgers et al. (2013) may
322 not be universally applicable (Stockley et al. 2017). Nevertheless, the potential for applying
323 alternative scattering corrections is allowed by including in the dataset the absorption values at

324 715 nm, $a_{t-w}(z,715)$, not corrected for the scattering offset ($a_{t-w}(z,715)$) would be zero when
325 corrected).

326 The additional correction for the finite acceptance angle of the detector, which would need
327 additional field measurements of the volume scattering phase function (Boss et al. 2009) not
328 included among the CoASTS and BiOMaP core data, could not be implemented.

329 In addition to regular instrument calibration and maintenance by the manufacturer,
330 systematic AC9s pure water ~~calibrations~~-offsets were determined during each CoASTS campaign
331 and, at the beginning and completion of each BiOMaP campaign in agreement with best
332 practices for field operation. This offset accounts for any instrument response change while the
333 AC9s are operated in their actual deployment configuration. The absorption and scattering
334 offsets between the reference manufacturer calibrations and those performed in the field were
335 applied as corrections values. In the presence of appreciable offsets between successive field
336 calibrations performed during the same campaign, differences were linearly interpolated over
337 time.

338 Automated quality control was applied to each data record to verify the spectral and spatial
339 (*i.e.*, vertical) consistency aiming at identifying those measurements affected by perturbations
340 caused by bubbles or large particles flowing into the AC9 measurement chambers (*i.e.*, mostly
341 individual spikes independently affecting $c_{t-w}(z,\lambda)$ or $a_{t-w}(z,\lambda)$ measurements especially in the
342 surface layer). Specifically, $c_{t-w}(z,\lambda)$ and $a_{t-w}(z,\lambda)$ spectra exhibiting pronounced differences
343 with respect to those characterizing the mean of profile spectra determined through a spectral
344 consistency test, or pronounced changes with respect to depth at any λ identified through a
345 spatial consistency test, were removed. The statistical parameters characterizing such a filtering
346 process were tuned for profile data typical of individual campaigns in view of minimizing the
347 potential for removing valid measurements.

348 The quality controlled $c_{t-w}(z,\lambda)$ and $a_{t-w}(z,\lambda)$ data were successively binned at 1 m
349 resolution and retained when the depth d_b assigned to the center of the bin determined from the
350 mean of the actual depths of individual measurements satisfies the condition $d_b = d_n \pm 0.25 \cdot d_i$,
351 where d_n is the nominal depth of the center of the bin and d_i the bin width.— The $c_{t-w}(\lambda)$ and
352 $a_{t-w}(\lambda)$ –values included in the CoASTS-BiOMaP dataset are the binned values tentatively
353 corresponding to an average depth of 1 m.

354 A minimum uncertainty of 0.005 m^{-1} is assumed to affect AC9 measurements
355 (Twardowski *et al.* 2001). Still, Stockley et al. (2017) showed that these values are largely
356 underestimated especially in highly scattering waters in the blue-green spectral bands.

358 **4.3 Backscattering from profile data**

359 *In situ* vertical profiles of backscattering coefficients $b_b(z,\lambda)$ were determined using
360 measurements performed with HydroScat-6 instruments from HOBI Labs Inc. (Tanque Verde,
361 Arizona) in six bands 10 nm wide at the 442, 488, 510, 555, 620 and 676 (or 671) nm center-
362 wavelenghts. In the absence of any advanced and consolidated processing for HydroScat-6
363 measurements, the values of $b_b(z,\lambda)$ were derived applying the conversion factor $\chi=1.08$ to
364 measurements of the volume scattering function $\beta(z,\psi,\lambda)$ performed at the sole scattering angle
365 $\psi=140^\circ$ (Maffione and Dana 1997). The derived backscattering values were successively
366 corrected for the water scattering and absorption applying the factor

$$368 \quad \sigma_C(z, \lambda) = \exp[k_e(\lambda)(a(z, \lambda) + 0.4b(z, \lambda))] \quad (4)$$

369

370 where $a(z,\lambda)$ and $b(z,\lambda)$ (with $b(z,\lambda)=c(z,\lambda)-a(z,\lambda)$) were obtained from AC9 measurements
 371 adding the pure water absorption and scattering coefficients, respectively, while the instrument
 372 specific spectral factors $k_e(\lambda)$ were those determined by the manufacturer during the initial
 373 calibration. Salinity corrections were applied considering ‘Fresh water’ b_{bw} from Morel (1974)
 374 for the Black Sea and Baltic Sea measurements, and the ‘Salt water’ b_{bw} from Morel (1974) for
 375 the other measurements. This solution, with respect to the use of actual salinity values, may lead
 376 to misestimates of b_{bb} , generally not exceeding 2% at 443 nm for the Baltic Sea and Black Sea.

377 Equivalent to AC9 measurements, automated quality control was also applied to $b_b(z,\lambda)$
 378 data to remove measurements exhibiting poor spectral and spatial (*i.e.*, vertical) consistency (*i.e.*,
 379 mostly individual spikes affecting $b_b(z,\lambda)$ at a single λ). By tuning the parameters defining the
 380 filtering process, spectra of $b_b(z,\lambda)$ exhibiting extreme differences with respect to the mean of
 381 profile spectra, or very high changes with depth at any λ , were removed. Quality controlled
 382 $b_b(z,\lambda)$ data were also binned at 1 m resolution adopting the same criteria applied for $a(z,\lambda)$ and
 383 $c(z,\lambda)$. The $b_b(\lambda)$ values included in the CoASTS-BiOMaP dataset are the binned values
 384 tentatively corresponding to an average depth of 1 m.

385 The quality index defined by the difference between $b_b(488)$ and the corresponding value
 386 $b_{bw}(488)$ is included in the dataset to identify those measurements mostly collected in very
 387 clear waters challenged by measurement uncertainties. The values of $b_{bw}(488)$, set equal to
 388 0.001603 m^{-1} or alternatively equal to 0.001233 m^{-1} for the sole Black Sea and Baltic Sea data,
 389 were determined from those provided in Morel (1974) fitted according to Twardowski et al.
 390 (2007).

391 Annual factory calibrations performed at HOBILabs were complemented by pre-field
 392 laboratory verifications performed at the JRC Marine Optical Laboratory. These laboratory
 393 verifications aimed at correcting for HysdroScat-6 response changes between factory
 394 calibrations.

395 Whitmire et al. (2007) estimated minimum uncertainties of 0.0007 m^{-1} for measurements of
 396 $b_{bp}(z,\lambda)$ (*i.e.*, $b_b(z,\lambda)$ minus the backscattering of pure water) performed with HydroScat-6
 397 instruments. Still, also in this case, actual uncertainties are expected to be much larger.

399 **4.4 Absorption of particulate matter determined from discrete water samples**

400 In vivo absorption coefficients $a_p(z,\lambda)$ of aquatic particles from water samples at discrete
 401 depths z were determined using the Transmission and Reflection ($T-R$) method proposed by
 402 Tassan and Ferrari (1995). This method was shown appropriate for any particle type, including
 403 highly back-scattering mineral particles or highly absorbing sediments. The method was
 404 implemented on a Perkin Elmer Lambda-19 and from 2004 on a Lambda-950, dual beam
 405 spectrometers equipped with integrating spheres.

406 Samples of particles were collected filtering water volumes on Whatman GF/F glass fibre
 407 filters with nominal pore size of $0.7\ \mu\text{m}$. Samples from the field were preserved in liquid
 408 nitrogen until laboratory analysis. The absorption coefficient $a_p(z,\lambda)$ of the equivalent particle
 409 suspension in the 400-750 nm spectral range with 1 nm resolution was determined from

$$411 \quad a_p(z,\lambda) = 2.3 A_s(z,\lambda) (F_a / V_w(z))^{-1} \quad (5)$$

412
 413 where $V_w(z)$ is the volume of filtered water, F_a the filter clearance area and $A_s(z,\lambda)$ the equivalent
 414 particle suspension absorbance obtained with the $T-R$ method.

415 The pigmented $a_{ph}(z,\lambda)$ and non-pigmented $a_{dp}(z,\lambda)$ fractions of the particulate absorption
416 coefficient $a_p(z,\lambda)$ were obtained bleaching the sample using a solution of sodium hypochlorite
417 (NaClO). The solution rapidly acts on pigment molecules and slowly on detritus making possible
418 a selective analysis of the two absorption components.- A description of the bleaching technique
419 is presented in Tassan and Ferrari (1995) and in Ferrari and Tassan (1999).

420 Focused studies on the accuracy of the $T-R$ method are given in Tassan and Ferrari
421 (1995) and in Tassan et al. (2000). Still, comprehensive uncertainty estimates for $a_{ph}(z,\lambda)$ and
422 $a_{dp}(z,\lambda)$ are not available. Nevertheless, dedicated analysis addressed the repeatability of in vivo
423 particulate absorption measurements performed with the $T-R$ method (see Zibordi et al. 2002).
424 These investigated: *i.* repeated analysis of the same sample (*i.e.*, each sample was analysed
425 twice) and *ii.* the analysis of duplicate samples (*i.e.*, duplicates obtained from the same water
426 volume). Results for repeated analysis of the same samples showed mean absolute percent
427 differences of $2.9\pm 2.3\%$ at 443 nm with mean $a_p(\bar{\varepsilon},443) = 0.082\pm 0.042 \text{ m}^{-1}$, increasing up to
428 $7.4\pm 6.0\%$ at 555 nm with mean $a_p(\bar{\varepsilon},555) = 0.023\pm 0.011 \text{ m}^{-1}$. These differences are attributed to:
429 *i.* method sensitivity, and *ii.* slight variations in the mechanical re-positioning of the sample in
430 front of the aperture of the integrating sphere combined with spatial non-homogeneities of the
431 particles distribution on the filter.

432 The analysis of duplicate samples showed mean absolute percentage differences of
433 $8.9\pm 5.9\%$ at 443 nm with mean $a_p(\bar{\varepsilon},443) = 0.090\pm 0.049 \text{ m}^{-1}$ and of $9.8\pm 7.0\%$ at 555 nm with
434 mean $a_p(\bar{\varepsilon},555) = 0.024\pm 0.012 \text{ m}^{-1}$. The former differences, increased by a few percent with
435 respect to those given for the repeated analysis of samples, are justified by: *i.* unavoidable
436 differences in replicates due to inhomogeneity affecting the particles distributions on filters; and
437 also *ii.* inhomogeneity in the distribution of particles in the water volumes used to produce the
438 samples. It is mentioned that an intrinsic error in the estimate of the actual particle absorption
439 coefficients results from the application of GF/F filters with nominal pore size of $0.7 \mu\text{m}$. In fact
440 these filters do not allow bacteria and the fraction of mineral particles with diameter lower than
441 $0.7 \mu\text{m}$ to be accounted for. However, the absorption of these small mineral particles is generally
442 negligible compared to the total absorption, while the absorption of bacteria is almost 10 times
443 lower than that of algal cells and 5–10 times lower than that of cyanobacteria (Morel and Ahn
444 1990). The $a_{ph}(z,\lambda)$ and $a_{dp}(z,\lambda)$ measurements included in the CoASTS-BiOMaP dataset refer to
445 water samples collected at approximately 1 m depth.

446

447 **4.5 Absorption of CDOM determined from discrete water samples**

448 The absorption coefficient $a_{ys}(z,\lambda)$ of CDOM at depth z was determined applying the
449 method detailed in Ferrari et al. (1996) using a Perkin Elmer Lambda-12 and from 2010 a
450 Lambda-35 dual-beam spectrometers. Samples were prepared by filtering water volumes on
451 Millipore $0.22 \mu\text{m}$ pore size cellulose filters and adding a solution of 10 gl^{-1} of NaN_3 to the
452 filtered water to prevent bacteria growth (typically 1 ml of the solution was added to 100 ml of
453 filtered water).

454 CDOM samples were preserved at approximately 4°C in an amber glass bottle until
455 laboratory analysis. The spectrometric measurements, generally carried out within a few days
456 from the completion of the measurement campaign, were performed with 1 nm resolution in the
457 350-750 nm spectral region. Measurements were performed placing a 10 cm quartz cuvette
458 containing pure milli-Q water in the optical path of the reference beam, and a 10 cm quartz
459 cuvette containing the CDOM sample in the optical path of the sample beam. It is acknowledged
460 that the 10 cm path-length systematically applied for the analysis of CoASTS and BiOMaP field

461 samples, naturally challenges the accuracy of measurements characterized by low CDOM
462 absorption such as those from the Eastern Mediterranean Sea.

463 The spectral absorption coefficient $a_{ys}(z,\lambda)$ was computed from the measured absorbance
464 $A_{ys}(z,\lambda)$ resulting from the difference between the sample absorbance and the reference
465 absorbance (Ferrari et al., 1996), as

$$467 a_{ys}(z,\lambda) = 2.3 A_{ys}(z,\lambda) L_c^{-1} \quad (6)$$

468
469 where L_c is the pathlength of the cuvette.

470 Assuming CDOM does not absorb in the red, The absorption coefficients are corrected
471 for the background offset by subtracting to $a_{ys}(z,\lambda)$ the mean of $a_{ys}(z,\lambda_i)$ spectral values for λ_i in
472 the 670-680 nm interval.

473 Comprehensive uncertainty values are also not available for $a_{ys}(z,\lambda)$. Still, the
474 repeatability of $a_{ys}(z,\lambda)$ measurements (see Zibordi et al. 2002) was also investigated through: *i.*
475 repeated analysis of the same samples; and *ii.* the analysis of duplicate samples. The repeated
476 analysis of the same samples showed average absolute percent differences varying as a function
477 of the absorption value from $10.1 \pm 7.3\%$ at 412 nm with mean $a_{ys}(z,412) = 0.168 \pm 0.037 \text{ m}^{-1}$ up to
478 $24.2 \pm 19.8\%$ at 555 nm with mean $a_{ys}(z,555) = 0.015 \pm 0.005 \text{ m}^{-1}$. These differences are mostly
479 ascribed to the precision of the method. The analysis of the duplicate samples showed expected
480 augmented average absolute percent differences when compared to repeated analysis of samples,
481 varying from $12.1 \pm 6.3\%$ at 412 nm with mean $a_{ys}(z,412) = 0.175 \pm 0.038 \text{ m}^{-1}$ and up to
482 $30.3 \pm 23.8\%$ at 555 nm with mean $a_{ys}(z,555) = 0.018 \pm 0.005 \text{ m}^{-1}$. The latter increased values are
483 largely justified by differences between samples.

484 It is finally mentioned that the use of $0.22 \mu\text{m}$ pore size filters to produce CDOM
485 samples, when the $0.7 \mu\text{m}$ pore size filters are applied for the quantification of particle
486 absorption coefficients, suggests that the overall absorption budget cannot be fully resolved. In
487 fact, as already anticipated, bacteria and very small mineral particles having size between 0.2 and
488 $0.7 \mu\text{m}$, are not included in the absorption analysis. Still, this missing contribution to the overall
489 absorption budget is expected to be minor.

490 As per $a_{ph}(\lambda)$ and $a_{dp}(\lambda)$, also the $a_{ys}(\lambda)$ measurements included in the CoASTS-BiOMaP
491 dataset refer to water samples collected at approximately 1 m depth.

493 **4.6 Pigments concentration**

494 Phytoplankton pigment concentrations were determined by using High Performance Liquid
495 Chromatography (HPLC) with the method proposed by Van Heukelem and Thomas (2005).
496 Exceptions are the samples collected before 2000 for which the method proposed by Jeffrey et al.
497 (1997) was applied.

498 The analysis were performed on samples of particulate matter retained on GF/F filters with a
499 nominal pore size of $0.7 \mu\text{m}$: this choice is justified by the diameter of living phytoplankton cells
500 generally higher than $1 \mu\text{m}$ (Stramsky and Kiefer, 1991). After filtration, samples were preserved
501 in liquid nitrogen until laboratory analysis.

502 Following Van Heukelem and Thomas (2005), the samples were transferred to vials with 3
503 ~~mL~~-mL 95% acetone and vitamin E as internal standard. Samples were then disrupted using a
504 vortex mixer, sonicated on ice, extracted at 4°C for 20 h, and mixed again. The samples were
505 successively filtered through $0.2 \mu\text{m}$ Teflon syringe filter into HPLC vials and placed in the
506 cooling rack of the HPLC system. Buffer and sample were injected in the HPLC (Shimadzu LC-

507 10A or alternatively an HP-1100, systems) in the 5/2 ratio using a pre-treatment program and
508 mixing in the loop before injection.

509 The list of pigments systematically analysed at the JRC Marine Optical Laboratory or
510 alternatively at DHI A/S (Hørsholm, Denmark) includes: chlorophyll a (resulting from the sum
511 of divinyl- and monovinyl-chlorophyll a), chlorophyll b, chlorophyll c₁+c₂, chlorophyllide a,
512 fucoxanthin, diadinoxanthin, β-carotene, zeaxanthin, alloxanthin, 19'-butanoyloxyfucoxanthin,
513 19'-hexanoyloxyfucoxanthin and diatoxanthin.

514 Various inter-comparisons of HPLC methods performed within the framework SeaWiFS
515 HPLC Analysis Round-Robin Experiments (SeaHARRE) organized by NASA with the JRC
516 participation, demonstrated the capability of various laboratories to achieve differences lower
517 than 6% in the determination of total chlorophyll *a* concentration *Chla* (*i.e.*, the sum of
518 chlorophyll *a* and chlorophyllide *a*) and lower than 25% for the other ancillary pigments
519 characterizing marine waters (Hooker et al. 2010). The analysis of CoASTS and BiOMaP shows
520 *Chla* values always higher than 0.03 - 0.04 μg l⁻¹. This may suggest some quantification limit for
521 the methodology applied to determine pigments concentration.

522 Consistent with $a_{ph}(z,\lambda)$, $a_{dp}(z,\lambda)$ and $a_{vs}(z,\lambda)$, measurements of *Chla* were performed on
523 water samples collected at approximately 1 m depth.

524

525 4.7 Suspended particulate concentration

526 The concentration of suspended particulate matter, *SPM*, was obtained from the net weight
527 of the particulate material collected on filters following the method detailed in Van der Linde
528 (1998) as an evolution of that proposed by Strickland and Parsons (1972). Samples were
529 produced by filtering volumes of water on GF/F filters with 0.7 μm nominal pore size previously
530 baked at 450 °C for 1 hour, pre-washed, dried for 1 hour at 75 °C and finally pre-weighed on a
531 electrobalance. After water filtration, the filters (*i.e.*, filtration area and border) were washed
532 with distilled water and stored at -18 °C for successive laboratory analysis. Before final
533 weighting, the filters were dried at 75 °C for 1 hour, and then temporarily stored in a desiccator.

534 The concentration of *SPM* was calculated from

535

$$536 \quad TSM_{SPM}(z) = [(W_f(z) - W_s(z)) - w_b] V(z)^{-1} \quad (7)$$

537

538 where $W_f(z)$ is the weight of the filter before filtration, $W_s(z)$ is the weight of the filter after
539 filtration, $V(z)$ is the volume of the filtered water and w_b is a correction term introduced to
540 account for variations in the weight of the filter sample due to changes in environmental
541 conditions between the two weightings steps. The values of w_b were determined from 'blank'
542 filters (*i.e.*, GF/F filters completely conditioned, not used for water filtration, but exposed to the
543 same processes of the sample filters: transportation to the measurement site and back, storage in
544 the freezer, drying). The w_b values applied in Eq. 7, are the differences between the average final
545 weight of 'blank' filters and their original average weight.

546 *SPM* values included in the CoASTS-BiOMaP data set are generally obtained from the
547 average of duplicate samples. In the case of large differences between duplicates (*i.e.*, tentatively
548 exceeding 20%) the *SPM* value from one of the two samples is used prior investigating the
549 surface and integrity of the samples, and also verifying the consistency of their values with AC9
550 measurements from close stations.

551 The use of GF/F filters with 0.7 μm nominal pore size for *SPM* analysis leads to an
552 underestimate of total suspended matter due to the loss of particles with diameter lower than 0.7

553 μm . However, it is recognized that the filter rinsing for salt removal and the filter conditioning
554 after filtration before final weighting, can induce errors certainly much larger than the mass of
555 particles with diameter lower than $0.7 \mu\text{m}$.

556 An analysis of measurement repeatability performed with duplicate samples showed mean
557 percent difference equal to $13.9 \pm 13.4\%$ with mean $SPM(z) = 0.86 \pm 0.40 \text{ mg}\cdot\text{l}^{-1}$. The largest
558 differences between duplicate samples (*i.e.*, larger than 30%) were observed with values of
559 $SPM(z)$ lower than approximately $0.5 \text{ mg}\cdot\text{l}^{-1}$. This is explained by the intrinsic uncertainty
560 affecting sample preparation (*i.e.*, water sample non-homogeneity and filter rinsing).

561 As for other quantities determined from the analysis of water samples, also the SPM values
562 included in the CoASTS-BiOMaP dataset refer to samples collected at approximately 1 m depth.

563

564 **4.8 Salinity and temperature**

565 Profiles of salinity $S_w(z)$ and temperature $T_w(z)$ measurement were performed with SBE
566 19-plus Conductivity-Temperature-Depth (CTD) sensors from Sea-Bird Scientific (Bellevue,
567 Washington). These devices were calibrated by the manufacturer approximately on a two-year
568 basis. Uncertainties are tentatively expected to be within $0.01\text{-}\text{‰}$ for salinity and 0.01°C for
569 temperature.

570 Equivalent to $a(z,\lambda)$, $c(z,\lambda)$ and $b_b(z,\lambda)$ profiles, automated quality control was also
571 applied to $S_w(z)$ and $T_w(z)$ data to remove measurement artefacts. By trimming filtering parameters
572 to individual campaigns, values of $S_w(z)$ and $T_w(z)$ exhibiting extreme changes with respect to
573 depth, were removed. Quality checked $S_w(z)$ and $T_w(z)$ data were binned at 1 m resolution
574 adopting the same criteria already applied for $a(z,\lambda)$, $c(z,\lambda)$ and $b_b(z,\lambda)$ - The values associated
575 with the first bin, tentatively representing the 1 m depth, are included in the CoASTS-BiOMaP
576 dataset.

577

578 **4.9 Meteorological and environmental observations**

579 Among the meteorological quantities and observations recorded during each measurements
580 station, the wind speed W_s , sea state S_s and cloud cover C_c are included in the data set.

581

582 **5. The near-surface CoASTS and BiOMaP dataset (CoASTS-BiOMaP)**

583 CoASTS-BiOMaP data are accessible at <https://doi.org/10.1594/PANGAEA.971945> in
584 tabular form and include the near-surface data products from CoASTS and BiOMaP
585 measurements of relevance for the validation of satellite ocean color data and the development of
586 bio-optical algorithms. All spectral data products are restricted to the nominal center-
587 wavelengths 412, 443, 490, 510, 555, 665 nm, unless diversely specified. CoASTS data products
588 are only provided from December 1998 when full standardization of measurements and
589 processing was put in place.- In addition, station data were excluded from CoASTS-BiOMaP
590 when the $L_{WN}(\lambda)$ or $K_d(\lambda)$ radiometric products did not satisfy basic quality control criteria by
591 exhibiting spectra with unexplained shape or amplitude. Furthermore, poor quality of data
592 products other than radiometric, implied the exclusion of their individual values from the dataset.

593 Table 3 provides a comprehensive list of the quantities included in the CoASTS-BiOMaP
594 dataset: each one is identified by a convenient symbol, a brief description and its physical units.
595 A summary of the average values of the major bio-optical and hydrographic quantities
596 determined for the various marine regions is provided in Table 4. These are: the diffuse
597 attenuation coefficient K_d at 490 nm, the water absorption coefficient (from discrete sample

598 analysis, pure water contribution excluded) $a_{\text{at } 490 \text{ nm}}$, the backscattering coefficient (water
599 contribution included) b_b , at 488 nm; the concentrations of total chlorophyll-a $Chla$ and
600 suspended particulate matter SPM; and the salinity S_w . All quantities exhibit ample differences
601 across the various marine regions. Notable, variations in $K_d(490)$ exceed one order of magnitude
602 between the Eastern Mediterranean (EMED) and the Baltic Sea (BLTS) waters (*i.e.*, $K_d(490)$
603 varies from 0.037 to 0.494 m^{-1}).

604 Figure 3 displays BioMaP and CoASTS $L_{\text{WN}}(\lambda)$ spectra for the different marine regions.
605 These spectra clearly indicate diverse bio-optical features for the different regions.- They span
606 from the highly oligotrophic Eastern Mediterranean Sea (EMED) showing maximum values in
607 the blue region, to the optically complex Baltic Sea (BLTS) dominated by the presence of high
608 concentrations of CDOM as expressed by low values of L_{WN} in the blue spectral region. Between
609 these, there are marine regions exhibiting diverse bio-optical complexity due to different
610 concentrations of optically significant constituents. Notably, some spectra from the North Sea
611 (NORS) indicate the presence of relatively high concentration of sediments, while spectra from
612 the Black Sea (BLK) and the northern Adriatic Sea (AAOT) suggest bio-optical conditions
613 determined by the presence of various concentrations of SPM and CDOM determining L_{WN}
614 maxima at the 510 or 555 nm center-wavelengths.

615 Table 5 provides the mean spectral values and related standard deviations of $Q_n(\lambda)$ for the
616 various marine regions as determined from radiometric profiles performed during near clear sky
617 conditions determined by $C_c \leq 1/4$. These naturally exhibit some spectral dependence varying
618 with the water type. For instance, $Q_n(\lambda)$ from the Eastern Mediterranean Sea (EMED) exhibit
619 almost spectrally constant mean values approaching 4 sr in the 412-555 nm spectral interval and
620 of approximately 5 sr at 665 nm. Conversely, regions such as the northern Adriatic Sea (AAOT)
621 exhibit mean values approaching 4.5 sr with some spectral dependence in the 412-555 nm
622 spectral region, and also a mean value of 5 sr at 665 nm.

623 Figure 4 displays the $a_{\text{ph}}(\lambda)$ spectra for the CoASTS and BioMaP regions. Notable is the
624 increase in the values of mean $a_{\text{ph}}(443)$ from 0.007 m^{-1} for the Eastern Mediterranean Sea
625 (EMED) to 0.191 m^{-1} and 0.220 m^{-1} for the Baltic Sea (BLTS) and North Sea (NORS),
626 respectively. The peculiar spectra shown by North Sea stations off the Belgian coast exhibiting
627 a_{ph} values higher at 412 nm than at 443 nm (see panel for NORS data in Fig. 4), are explained by
628 high concentrations of pheophytin leading to an increase of the absorption coefficient toward 412
629 nm.

630 Figure 5 displays the comparison of the near surface absorption coefficients (pure water
631 excluded) determined from AC9 measurements at the center-wavelength of 443 nm, $a_{\text{t-w}}(\text{AC9})$,
632 versus the equivalent absorption coefficients determined from water samples, $a_{\text{t-w}}(\text{sample}) =$
633 $a_{\text{ph}}(443) + a_{\text{di}}(443) + a_{\text{ys}}(443)$. Results suggest an increasing underestimate of $a_{\text{t-w}}(\text{AC9})$ and larger
634 relative scattering with a decrease in absorption. This is highlighted by the scatter plots of data
635 from the Eastern Mediterranean Sea (EMED) exhibiting an underestimate exceeding 70% with
636 values of $a_{\text{t-w}}(\text{samples})$ generally lower than 0.1 m^{-1} . Conversely, the Baltic Sea (BLTS) shows
637 outstanding agreement between the compared quantities with absorption values comprised in the
638 range of 0.2-1.2 m^{-1} . These mean differences between $a_{\text{t-w}}(\text{AC9})$ and $a_{\text{t-w}}(\text{samples})$ absorption
639 values could be explained by an incomplete correction of the perturbing effects due to finite
640 acceptance angle of the detector, the non-fully reflective surface of the AC9 absorption chamber
641 (*i.e.*, the two short 25 cm path-length tubes) and also by the non-negligible absorption of
642 particles at the reference wavelength $\lambda_0 = 715 \text{ nm}$ applied for scattering corrections.

643

644
645
646
647
648

649 Table 3. The CoASTS-BiOMaP data set: quantities identified by symbols, description of
650 quantities and related units.

<i>Symbol</i>	<i>Description</i>	<i>Units</i>	<i>Details</i>
<i>Station ID</i>	Station identifier	Code	<i>Gccssit</i> ⁽¹⁾
<i>Date&Time</i>	Date and time	GMT	<i>yyyy-mm-ddTThh:mm:ss</i> ⁽²⁾
<i>Lon</i>	Longitude	Degrees	
<i>Lat</i>	Latitude	Degrees	
<i>Sz</i>	Sun zenith	Degrees	
<i>Sa</i>	Sun azimuth	Degrees	
$L_u(\lambda)$	Upwelling radiance at depth 0 ⁻	W m ⁻² nm ⁻¹ sr ⁻¹	<u>At nominal λ_s⁽³⁾</u>
$E_d(\lambda)$	Downward irradiance at depth 0 ⁻	W m ⁻² nm ⁻¹	<u>At nominal λ_s⁽³⁾</u>
$E_u(\lambda)$	Upward irradiance at depth 0 ⁻	W m ⁻² nm ⁻¹	<u>At nominal λ_s⁽³⁾</u>
$K_t(\lambda)$	Diffuse att. coeff. from $L_u(z,\lambda)$	m ⁻¹	<u>At nominal λ_s⁽³⁾</u>
$K_d(\lambda)$	Diffuse att. coeff. from $E_d(z,\lambda)$	m ⁻¹	<u>At nominal λ_s⁽³⁾</u>
$K_u(\lambda)$	Diffuse att. coeff. from $E_u(z,\lambda)$	m ⁻¹	<u>At nominal λ_s⁽³⁾</u>
$E_s(\lambda)$	Downward irradiance at depth 0 ⁺	W m ⁻² nm ⁻¹	<u>At nominal λ_s⁽³⁾</u>
$Q_n(\lambda)$	Q -factor an nadir at depth 0 ⁻	sr	<u>At nominal λ_s⁽³⁾</u>
$R_{RS}(\lambda)$	Remote sensing reflectance at depth 0 ⁺	sr ⁻¹	<u>At nominal λ_s⁽³⁾</u>
$L_{WN}(\lambda)$	Normalized water-leaving rad. at depth 0 ⁺	W m ⁻² nm ⁻¹ sr ⁻¹	<u>At nominal λ_s⁽³⁾</u>
$Q_R(412)$	Ratio of $Q_n(412)$ at depth 0 ⁻ to $Q_n(1,412)$ at 1 m <u>depth</u>	–	<u>Introduced to best support the use of $Q_n(\lambda)$ (large deviations from 1 may indicate extrapolation issues)</u>
$R_d(412)$	Ratio of the diffuse $E_d(412)$ to direct [$E_s(412) - E_d(412)$] above-water downward irradiance at 412 nm	–	
$CV E_s(412)$	Coefficient of variation $E_s(412)$	%	
$R(412)$	Ratio of the <u>above-water downward irradiance</u> $E_s(412)$ to the <u>in-water downward irradiance</u> $E_d(412)$ multiplied by 1.04	–	
$K_t(490)$	Diffuse attenuation <u>coefficient</u> $K_d(490)$ minus the diffuse attenuation coefficient of pure sea water $K_w(490)$ <u>assumed constant and equal to 0.0212</u>	m ⁻¹	<u>Introduced to best support the exploitation of data (a negative value may suggest extrapolation challenged by wave perturbations)</u>
$a_{ph}(\lambda)$	Abs <u>orption</u> coeff <u>icient</u> by pigmented particles at <u>1 m depth</u>	m ⁻¹	<u>At nominal λ_s⁽³⁾</u>
$a_{dt}(\lambda)$	<u>Absorption coefficient</u> by non-pigmented part. at <u>1 m depth</u>	m ⁻¹	<u>At nominal λ_s⁽³⁾</u>
$a_{ys}(\lambda)$	<u>Absorption coefficient</u> by CDOM at <u>1 m depth</u>	m ⁻¹	<u>At nominal λ_s⁽³⁾</u>
$a_{t-w}(\lambda)$	<u>Absorption coefficient</u> from AC9 at <u>1 m depth</u>	m ⁻¹	<u>At AC9 λ_s⁽⁴⁾. The values $a_{t-w}(715)$ are not corrected for the scattering</u>

				offset. If corrected, their values would be zero.
$c_{t-w}(\lambda)$		Beam attenuation coefficient from AC9 at 1 m depth	m^{-1}	At AC9 $\lambda_s^{(4)}$
$b_b(\lambda)$		Backscattering coefficient from HydroScat-6 at 1 m depth	m^{-1}	At HydroScat-6 $\lambda_s^{(5)}$
$b_b(488) - b_{bw}(488)$		Backscattering coefficient $b_b(488)$ minus the backscattering coefficient of pure sea water $b_{bw}(488)$ assumed constant and equal to $0.001603 m^{-1}$ or alternatively $0.001233 m^{-1}$ for the sole Black Sea and Baltic Sea measurements	m^{-1}	Introduced to best support the exploitation of data (a negative value may indicate measurements challenged by significant uncertainties)
<i>Chla</i>		Total chlorophyll- <i>a</i> concentration at 1 m depth ⁽⁶⁾	$\mu g l^{-1}$	
<i>TSMSPM</i>		Suspended particulate matter concentration at 1 m depth	$mg l^{-1}$	
T_w		Temperature of seawater at 1 m depth	$^{\circ}C$	
S_w		Salinity of seawater at 1 m depth	‰	
W_s		Wind speed	$m s^{-1}$	
S_s		Sea state	0-9	WMO scale
C_c		Cloud cover	0-4	Octa/2

651 ¹ *G* indicates the site or geographic region (*V* and *W* for AAOT, *A* for Adriatic Sea, *B* for Baltic Sea, *E* for Eastern
652 Mediterranean Sea, *K* for Black Sea, *L* for Ligurian Sea, *N* for North Sea, *O* for Western Mediterranean Sea, *I* for
653 Iberian Shelf, *P* for Greenland Sea), while *cc* indicates the campaign number for the specific region, *ss* the station
654 number and *ii* the cast number.

655 ² The letters *yyyy* indicate the year, *mm* the month, *dd* the day *hh*, the hours and *mm* the minutes.

656 ³ Nominal center-wavelengths for radiometric data products are 412, 443, 490, 510, 555 are 665 nm.

657 ⁴ Center-wavelengths for AC9 data products are 412, 440, 488, 510, 555, 630, 650, 676, and 715 nm.

658 ⁵ Center-wavelengths for HydroScat-6 data products are 442, 488, 510, 555, 620, and 676 (or 671) nm.

659 ⁶ Total chlorophyll-*a* concentration indicates the sum of chlorophyllide-*a*, monovinyl- and divinyl-chlorophyll-*a*.

660

661

662 Table 4. Mean \pm standard deviations of quantities describing the bio-optical and hydrographic
663 characteristics of the CoASTS and BioMaP marine regions: the diffuse attenuation coefficient K_d
664 [at 490 nm](#); the seawater absorption coefficient (excluding pure water contribution) *a* determined
665 from discrete sample analysis [at 490 nm](#); the backscattering coefficient (including pure water
666 contribution) b_b [at 488 nm](#); the concentrations of total chlorophyll-*a* *Chla* and suspended
667 [particulate](#) matter *SPM*; and finally the salinity S_w .

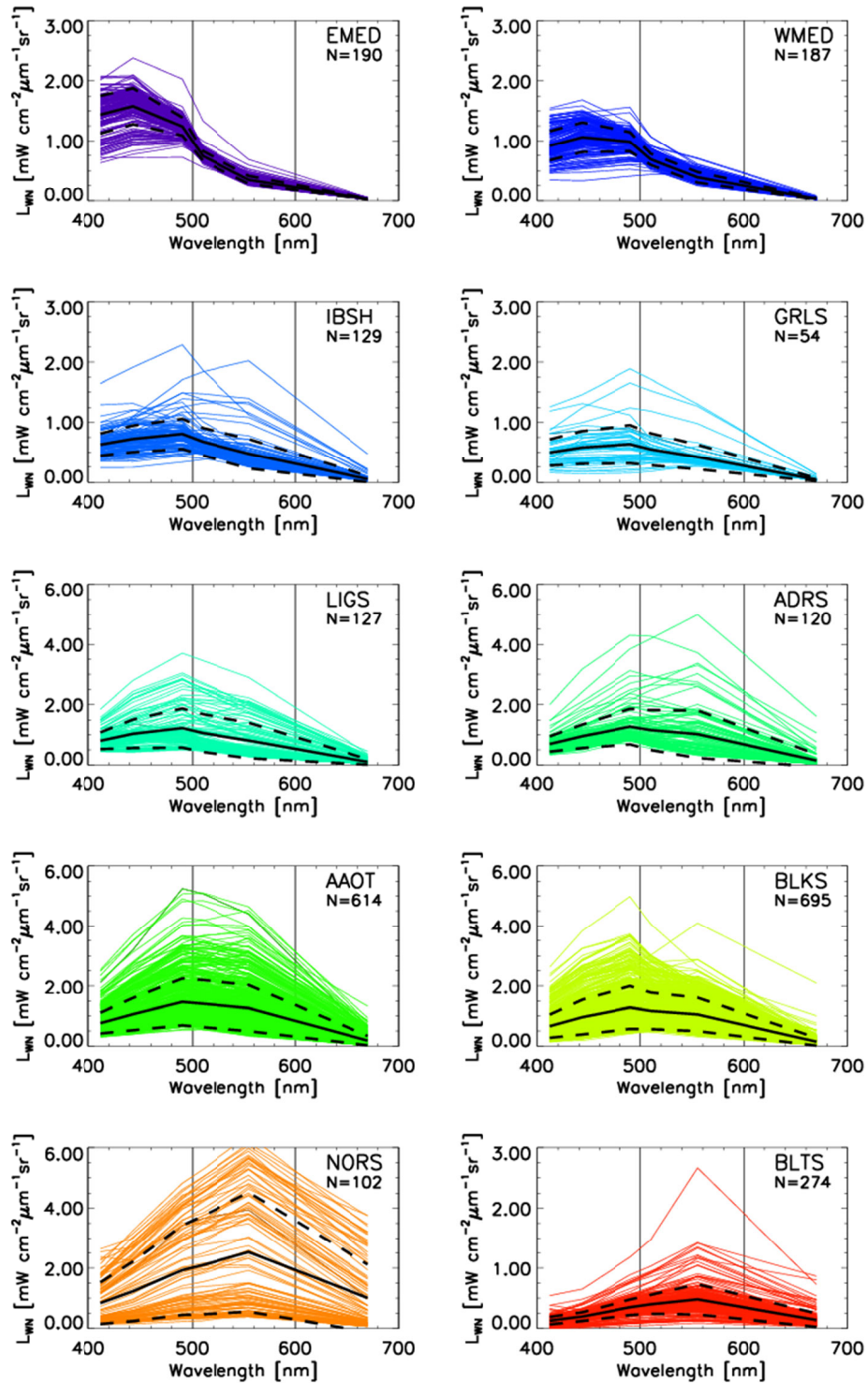
668

Region	$K_d(490)[m^{-1}]$	$a(490) [m^{-1}]$	$b_b(488)[m^{-1}]$	$Chla[\mu g l^{-1}]$	$SPM[mg l^{-1}]$	$S_w[\text{‰}]$
EMED	0.037 \pm 0. 022	0.031 \pm 0. 012	0.0026 \pm 0.0007	0.09 \pm 0.08	0. 27 \pm 0. 45	38. 6 \pm 0.7
WMED	0.046 \pm 0.025	0.040 \pm 0.019	0.0032 \pm 0.0009	0.30 \pm 0.37	0. 30 \pm 0.22	37.8 \pm 0.4
IBSH	0.084 \pm 0.049	0.073 \pm 0.033	0.0040 \pm 0.0023	0.81 \pm 0.83	0.53 \pm 0.39	36.0 \pm 0.2
GRLS	0.097 \pm 0.062	0.082 \pm 0.032	0.0039 \pm 0.0021	0.94 \pm 1.04	0.64 \pm 0.28	34.0 \pm 1.6
LIGS	0.110 \pm 0.079	0.079 \pm 0.045	0.0078 \pm 0.0067	0.93 \pm 0.85	0.71 \pm 0.57	37.7 \pm 1.0
ADRS	0. 141 \pm 0.125	0.085 \pm 0.059	0.0090 \pm 0.0067	1.25 \pm 1.32	1.14 \pm 1.45	35.6 \pm 2.3
AAOT	0.176 \pm 0.102	0.099 \pm 0.053	0.0121 \pm 0.0073	1.28 \pm 1.13	1.25 \pm 0.76	34.9 \pm 2.3

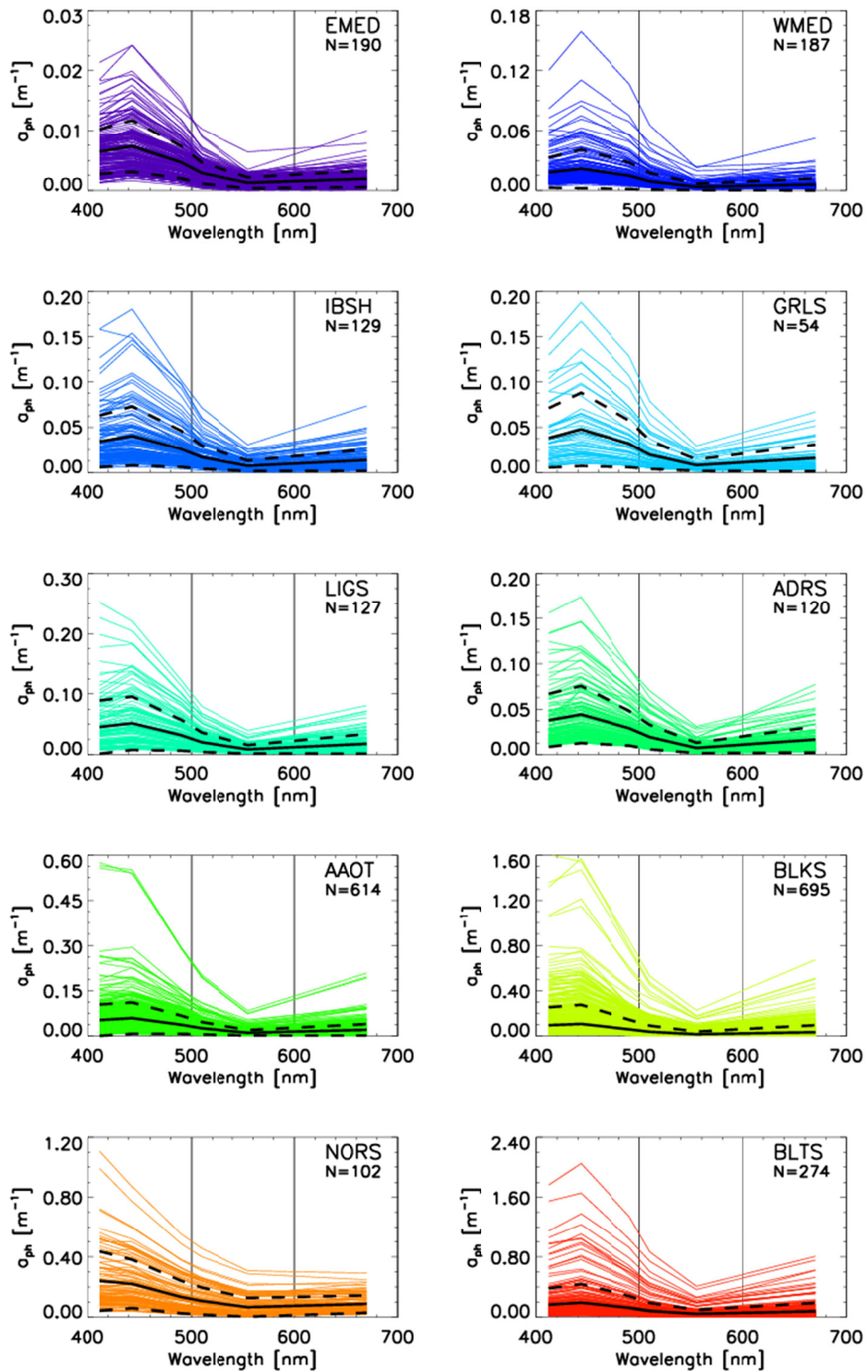
BLKS	0.219±0.254	0.131±0.130	0.0093±0.0066	1.62±3.13	1.17±1.24	16.6±1.8
NORS	0.876±0.864	0.377±0.346	0.0197±0.0160	4.23±2.27	9.96±12.52	33.7±1.4
BLTS	0.494±0.409	0.308±0.269	0.0107±0.0084	4.99±8.04	1.53±1.71	6.2±1.4

669

670

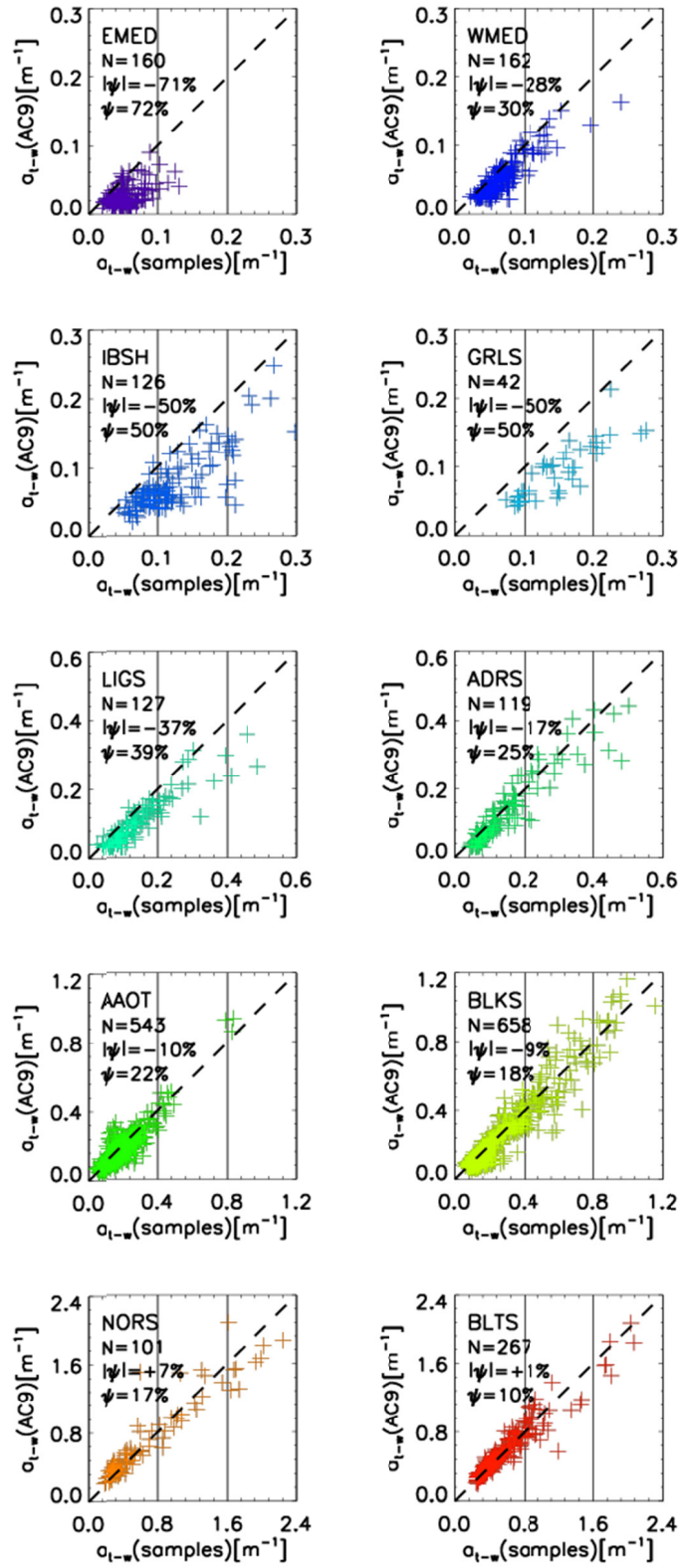


671
 672 Figure 3. Spectra of $L_{WN}(\lambda)$ for the CoASTS and BioMaP geographic regions (see Table 1 for
 673 acronyms). N indicates the number of spectra. The continuous black lines indicate mean values
 674 while the dashed lines indicate ± 1 standard deviation. For convenience, the spectra are plotted in
 675 units of $\text{mW cm}^{-2} \mu\text{m}^{-1} \text{sr}^{-1}$.



676

677 Figure 4. Spectra of $a_{ph}(\lambda)$ for the CoASTS and BioMaP marine regions. N indicates the number
 678 of spectra. The continuous black lines indicate mean values while the dashed lines indicate ± 1
 679 standard deviation.



680
681

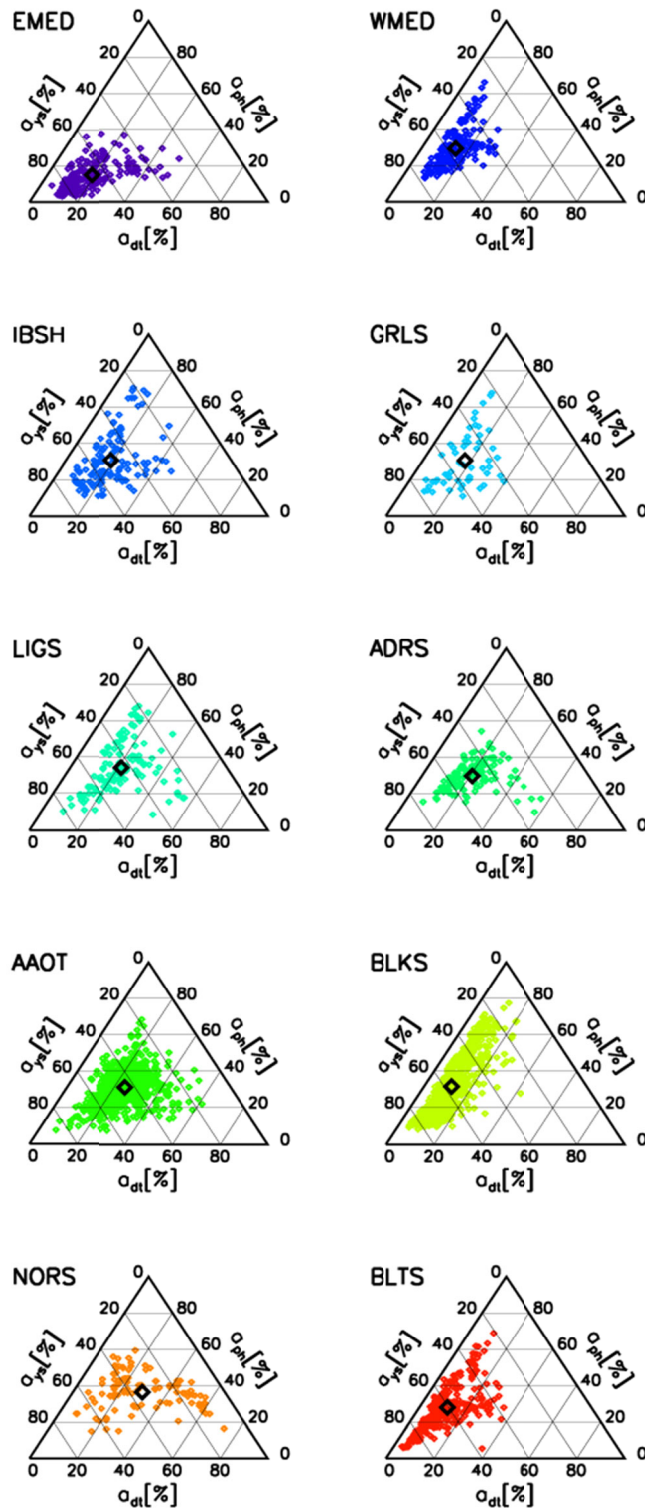
682 Figure 5. Scatter plot of AC9 derived $a_{t-w}(AC9)$ and laboratory measurements performed on
683 | water samples $a_{t-w}(\text{samples})$ of the water absorption coefficient (water excluded) determined at
684 | the 443 nm center-wavelength for the diverse CoASTS and BioMaP marine regions. N indicates
685 | the number of samples while $|\psi|$ and ψ indicate the mean of absolute (unsigned) percent
686 | differences and the mean of (signed) percent differences, respectively.

687
688
689 Table 5. Spectral values of $Q_n(\lambda)$ in units of sr at the 412, 443, 490, 510, 555 and 670 nm center-
691 | wavelengths for the CoASTS and BioMaP marine regions, determined from in-water radiometric
692 | profiles performed with cloud cover $C_C \leq 1/4$.

Region	412	443	490	510	555	670
EMED (N=127)	3.89±0.33	3.90±0.36	3.88±0.42	3.87±0.45	3.84±0.54	4.90±1.12
WMED (N=100)	4.08±0.36	4.14±0.41	4.20±0.46	4.21±0.48	4.19±0.52	4.96±0.76
IBSH (N=87)	4.18±0.37	4.22±0.38	4.26±0.43	4.26±0.45	4.24±0.51	4.58±0.59
GRLS (N=11)	3.97±0.33	4.08±0.37	4.14±0.38	4.12±0.37	4.00±0.34	4.18±0.38
LIGS (N=53)	4.52±0.40	4.54±0.36	4.57±0.36	4.59±0.38	4.66±0.44	5.14±0.58
ADRS (N=71)	4.47±0.65	4.39±0.57	4.33±0.54	4.34±0.55	4.40±0.62	4.98±0.95
AAOT (N=372)	4.56±0.56	4.43±0.51	4.33±0.49	4.33±0.50	4.41±0.58	5.02±0.84
BLKS (N=401)	4.51±0.54	4.49±0.57	4.47±0.59	4.47±0.59	4.47±0.59	5.06±0.80
NORS (N=27)	4.70±0.60	4.71±0.57	4.69±0.54	4.67±0.53	4.60±0.50	4.90±0.48
BLTS (N=87)	4.93±0.69	5.09±0.74	5.18±0.78	5.16±0.76	4.99±0.66	5.20±0.86

693
694
695 Figure 6 shows trilinear (ternary) plots of the absorption coefficients $a_{ys}(443)$, $a_{dt}(443)$ and
696 | $a_{ph}(443)$, expressed in percent of the total absorption (*i.e.*, with respect to $a_{ys}(443)+a_{dt}(443)+$
697 | $a_{ph}(443)$), displayed with values increasing in the counter-clockwise direction (Harris 1999).
698 | These results exhibit very few cases characterized by dominance of absorption by particles with
699 | a_{ph} and a_{dt} values close to the upper and lower right apexes, respectively. Conversely, most of the
700 | cases indicate dominance of absorption by coloured dissolved organic matter: see the a_{ys} values
701 | near the lower left apex). This is particularly evident for the oligotrophic waters of the Eastern
702 | Mediterranean Sea (EMED), and by the patterns characterizing the oligotrophic-mesotrophic
703 | waters of the Western Mediterranean Sea (WMED), the optically complex water of the Black
704 | Sea (BLKS) and the highly absorbing waters of the Baltic Sea (BLTS).

705 The specific results shown for the Mediterranean Sea (*i.e.*, EMED and WMED), which
706 | may suggest inconsistency with the definition of Case-1 waters (IOCCG 2000), are supported by
707 | an independent study from Pérez et al. (2016).
708



709

710 Figure 6. Trilinear (ternary) plots of the absorption coefficients a_{ys} , a_{dt} and a_{ph} expressed in
 711 percent of the total absorption (*i.e.*, with respect to $a_{ys}+a_{dt}+a_{ph}$) at the 443 nm center-wavelength.

712 | The empty black square indicates the mean of the plotted values.

713
714
715
716
717
718
719
720
721
722
723
724
725
726
727
728
729
730
731
732
733
734
735
736
737
738
739
740
741
742
743
744
745
746
747
748
749
750
751
752
753
754
755
756
757

Parameters determined from the exponential fit versus wavelength of $a_{dt}(\lambda)$ and $a_{ys}(\lambda)$, and the power law fit of $b_b(\lambda)$ versus wavelength, are provided in Tables 6-8. Specifically, the spectral values of $a_{dt}(\lambda)$ and $a_{ys}(\lambda)$ were fitted within the 412–665 nm spectral interval using

$$a_{dt}(\lambda) = A_{dt} \exp(-S_{dt}(\lambda - 412)) + B_{dt} \quad (8)$$

and

$$a_{ys}(\lambda) = A_{ys} \exp(-S_{ys}(\lambda - 412)) + B_{ys}, \quad (9)$$

where A_{dt} and A_{ys} indicate the absorption coefficients fitted at 412 nm, S_{dt} and S_{ys} the slope of the exponential function, and, B_{dt} and B_{ys} account for the background.

Conversely, the spectral values of $b_b(\lambda)$ at the center-wavelengths $\lambda=442, 488, 510, 550$ and 620 nm (excluding 676 or 6171 nm due to potential perturbations by fluorescence), were fitted using

$$b_b(\lambda) = A_b (\lambda/442)^{-S_b}, \quad (10)$$

where A_b indicates the backscattering coefficient at 442 nm and S_b the slope of the power law function.

Table 6 shows mean values of the slope S_{dt} varying from 0.009 nm^{-1} for the Eastern Mediterranean Sea (EMED) up to 0.013 for the North Sea (NORS). Values of the bias B_{dt} naturally increase with A_{dt} : the largest value of $B_{dt} = 0.067 \text{ m}^{-1}$ is observed for the North Sea (NORS) that also exhibits the highest value of $A_{dt} = 0.288 \text{ m}^{-1}$. Residuals R_{dt} , which also increase with A_{dt} , are quite minor suggesting a general good performance of the exponential fitting function.

Table 7 shows mean values S_{ys} varying from 0.012 nm^{-1} for the Eastern Mediterranean Sea (EMED) up to 0.019 nm^{-1} for the Baltic Sea (BLTS). The systematic negative biases B_{ys} across all marine regions are likely explained by the choice of zeroing the original spectra of absorption coefficients using values averaged in the 670-680 nm spectral interval. High residuals $B_{ys} = -0.029 \text{ m}^{-1}$ are observed for the Baltic Sea (BLTS). This is explained by a decreased performance of Eq. 9 when fitting spectra of absorption coefficients exhibiting values approaching or exceeding 1 m^{-1} at 412 nm. Still, all residuals B_{ys} expressed in percent of A_{ys} vary between 0.3 and 0.5%, except for the East Mediterranean Sea (EMED) showing a value of 0.9%.

As expected, also the values of S_b largely vary across the CoASTS and BiOMaP marine regions: in particular they exhibit values of $2.97 \mu\text{m}^{-1}$ for the East Mediterranean Sea (EMED), $2.06 \mu\text{m}^{-1}$ for the Iberian Shelf (IBSH) and $0.74 \mu\text{m}^{-1}$ for the North Sea (NORS). This is likely explained by an increase of the average particles size when going from the oligotrophic East Mediterranean Sea to the eutrophic and more sediment loaded North Sea.

Figure 7 and 8 shows the distribution of *Chla* and *SPM* across the CoASTS and BiOMaP marine regions. The very low concentrations characterizing the oligotrophic waters of the Eastern Mediterranean Sea (EMED) exhibiting mean *Chla* values of $0.09 \mu\text{g l}^{-1}$ and mean *SPM* values of 0.27 mg l^{-1} , are remarkable. Conversely, *Chla* exhibits mean values in the range of 4-5 $\mu\text{g l}^{-1}$ for both the North Sea (NORS) and Baltic Sea (BLKS), while for the same marine regions

758 *SPM* shows mean values of 9.96 and 1.53 mg l⁻¹, respectively. A log-normal distribution of both
 759 *Chla* and *SPM* is generally confirmed for the CoASTS and BiOMaP data-sets.

760 Figure 9 displays the scatter plots of $b_{bp}(488)/b_p(488)$ versus *Chla*, where $b_p(488)$ is
 761 determined by the difference between $c_{t-w}(488)$ and $a_{t-w}(488)$, while $b_{bp}(488)$ is determined from
 762 $b_p(488)$ by subtracting the scattering coefficient of water $b_w(488)$ from Morel (1974). Results are
 763 consistent with those shown by Twardowski et al. (2001) for a variety of experimental data, with
 764 $b_{bp}(488)/b_p(488)$ typically varying between 0.003 and 0.025. Exception are some very low
 765 values of $b_{bp}(488)/b_p(488)$ for EMED data likely explained by large measurement uncertainties.
 766 Coherent with published results is also the generally higher values and higher scatter of
 767 $b_{bp}(488)/b_p(488)$ in correspondence of low *Chla* concentrations.

770 Table 6. Parameters A_{dt} , S_{dt} and B_{dt} of the exponential fitting function (see Eq. 8) applied to the
 771 values of $a_{dt}(\lambda)$. The quantity R_{dt} indicates the spectral average of absolute differences (*i.e.*,
 772 residuals) between actual and fitted values.

Region	A_{dt} [m ⁻¹]	S_{dt} [nm ⁻¹]	B_{dt} [m ⁻¹]	R_{dt} [m ⁻¹]
EMED (N=190)	0.010±0.007	0.009±0.002	0.002±0.001	0.0000
WMED (N=186)	0.009±0.004	0.012±0.001	0.003±0.001	0.0000
IBSH (N=129)	0.024±0.022	0.011±0.001	0.006±0.005	0.0001
GRLS (N=54)	0.024±0.014	0.012±0.002	0.007±0.004	0.0000
LIGS (N=126)	0.032±0.026	0.011±0.002	0.007±0.004	0.0001
ADRS (N=120)	0.042±0.057	0.012±0.001	0.009±0.011	0.0000
AAOT (N=614)	0.048±0.031	0.012±0.001	0.009±0.005	0.0000
BLKS (N=692)	0.034±0.057	0.011±0.002	0.005±0.008	0.0001
NORS (N=102)	0.288±0.377	0.013±0.001	0.067±0.094	0.0005
BLTS (N=274)	0.095±0.125	0.011±0.002	0.011±0.017	0.0003

774
 775
 776
 777 Table 7. Parameters A_{ys} , S_{ys} and B_{ys} of the exponential fitting function (see Eq. 9) applied to the
 778 values of $a_{ys}(\lambda)$. The quantity R_{ys} indicates the spectral average of absolute differences (*i.e.*,
 779 residuals) between actual and fitted values.

Region	A_{ys} [m ⁻¹]	S_{ys} [nm ⁻¹]	B_{ys} [m ⁻¹]	R_{ys} [m ⁻¹]
EMED (N=182)	0.056±0.025	0.012±0.004	-0.005±0.007	0.0004
WMED (N=183)	0.059±0.019	0.013±0.003	-0.002±0.002	0.0002
IBSH (N=129)	0.093±0.036	0.014±0.003	-0.004±0.005	0.0004
GRLS (N=54)	0.107±0.027	0.014±0.003	-0.004±0.003	0.0003
LIGS (N=126)	0.091±0.052	0.014±0.004	-0.004±0.004	0.0004
ADRS (N=120)	0.114±0.058	0.016±0.002	-0.002±0.002	0.0003
AAOT (N=592)	0.132±0.059	0.017±0.004	-0.003±0.005	0.0003
BLKS (N=693)	0.205±0.122	0.017±0.002	-0.004±0.003	0.0005
NORS (N=102)	0.280±0.094	0.017±0.002	-0.004±0.002	0.0007
BLTS (N=274)	0.606±0.330	0.019±0.001	-0.004±0.003	0.0029

781
782

783 Table 8. Parameters A_b and S_b of the power law fitting function (see Eq. 10) applied to the values
784 of $b_b(\lambda)$ at $\lambda= 443, 488, 510, 555$ and 620 nm for the CoASTS and BioMaP marine regions. The
785 quantity R_b indicates the spectral average of absolute differences (*i.e., residuals*) between actual
786 and fitted data.

Region	A_b [m^{-1}]	S_b [μm^{-1}]	R_b [m^{-1}]
EMED (N= <u>184</u>)	0.0034 \pm 0.0008	2. <u>97</u> \pm 0. <u>56</u>	0.0001
WMED (N= <u>186</u>)	0.0041 \pm 0.0009	2. <u>54</u> \pm 0.42	0.0001
IBSH (N=127)	0.0051 \pm 0.0025	2.06 \pm 0.55	0.0002
GRLS (N= <u>52</u>)	<u>0.0048</u> \pm 0.0024	2.25 \pm 0.33	0.0001
LIGS (N=126)	0.0091 \pm 0.0072	1.83 \pm 0.64	0.0002
ADRS (N=111)	0.0103 \pm 0.0071	1.74 \pm 0.57	0.0002
AAOT (N=479)	0.0136 \pm 0.0078	1.35 \pm 0.42	0.0004
BLKS (N=534)	0.0126 \pm 0.0077	1.99 \pm 0.53	0.0006
NORS (N=57)	0.0207 \pm 0.0157	0.74 \pm 0.38	0.0005
BLTS (N=256)	<u>0.0118</u> \pm 0.0082	1.15 \pm 0.49	0.0003

787
788

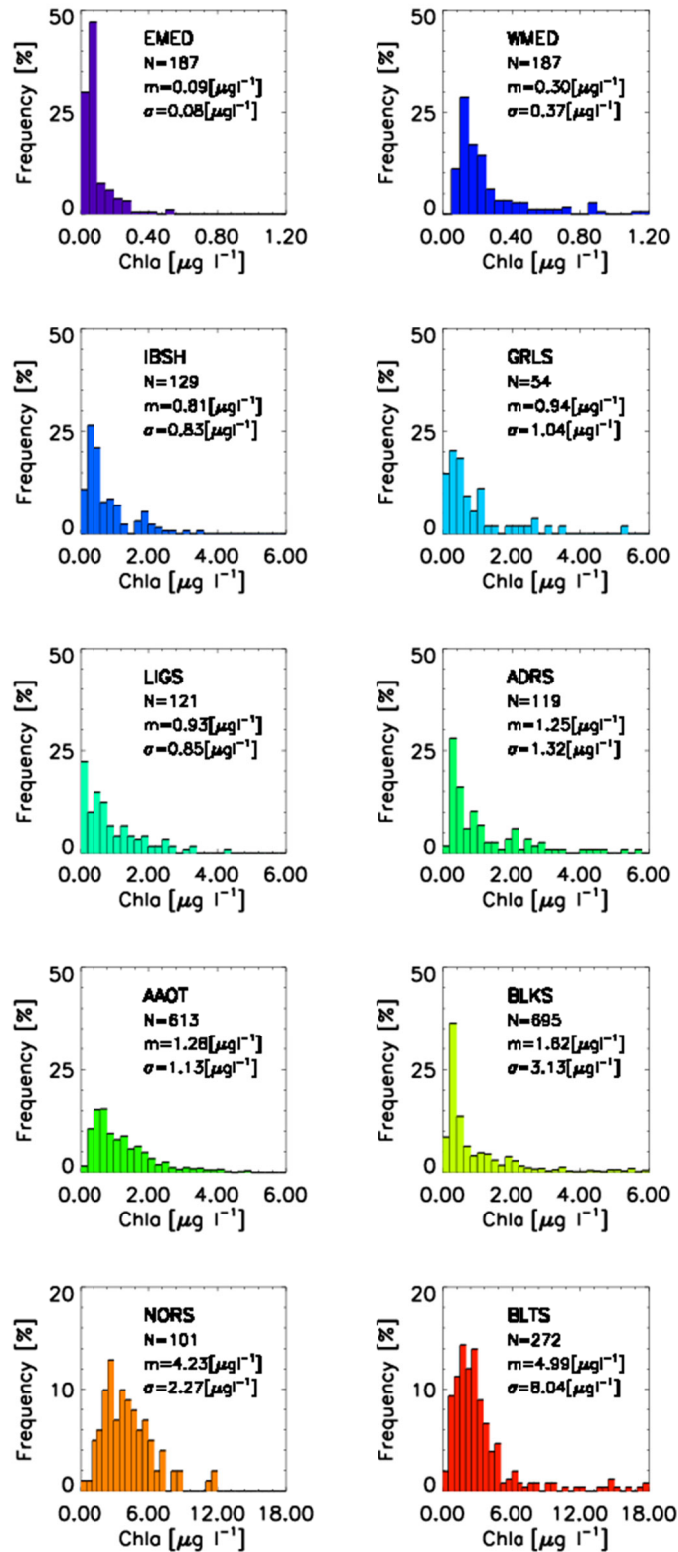
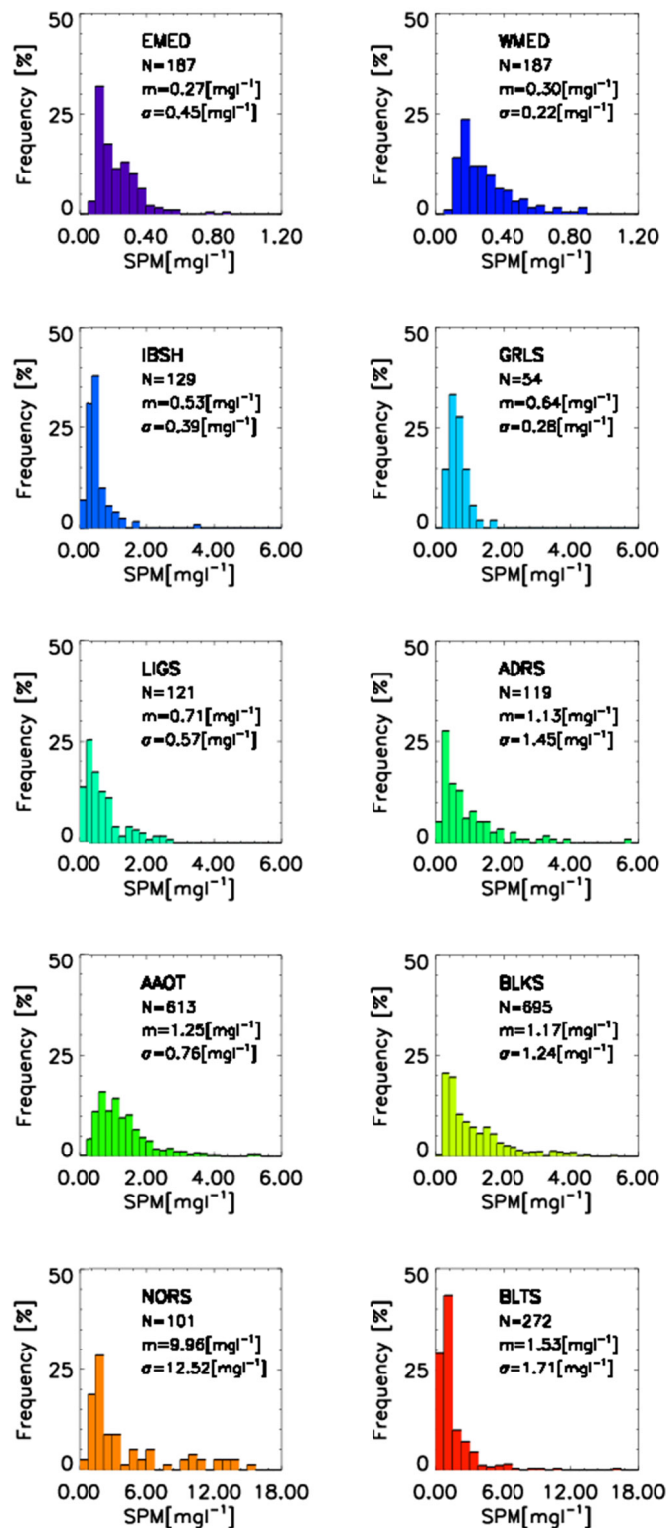


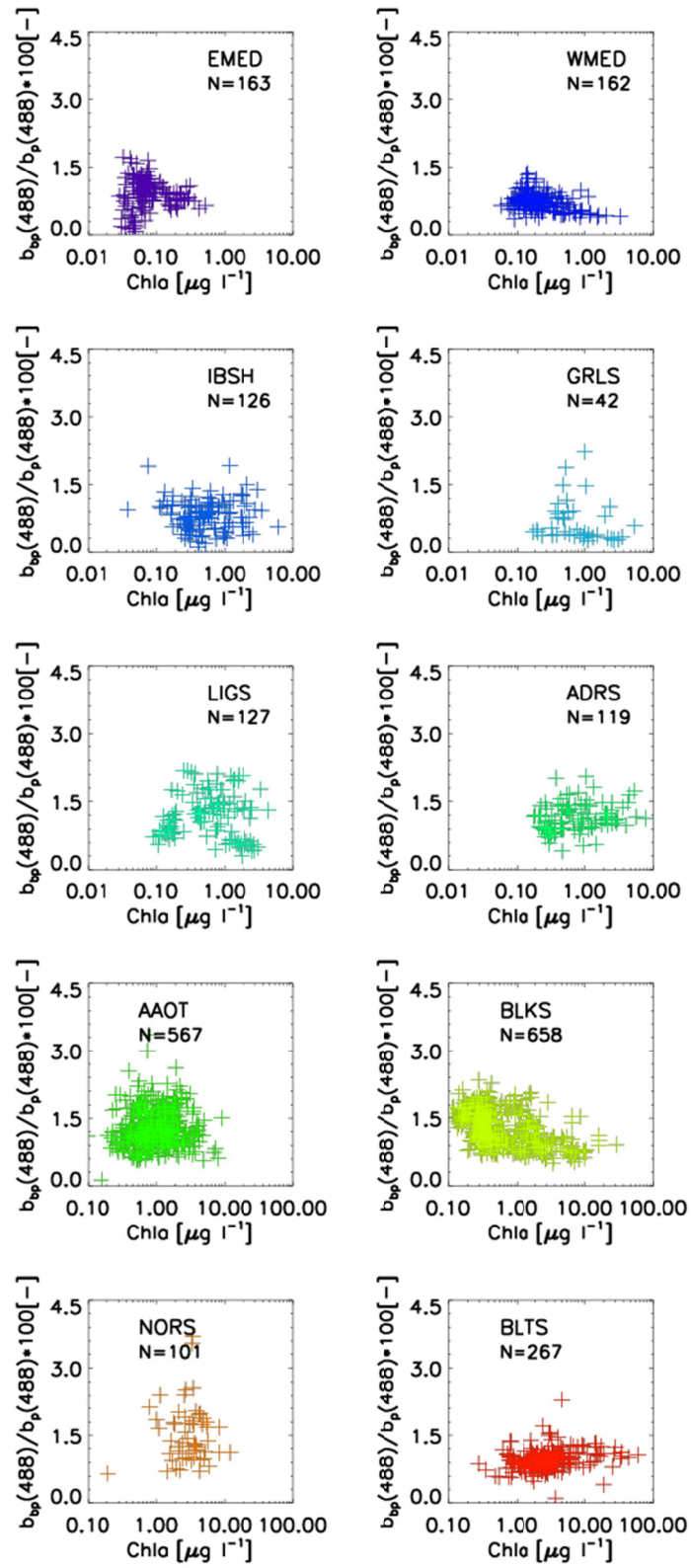
Figure 7. Frequency distribution of *Chla* across the CoASTS and BioMaP marine regions. N indicates the number of stations, *m* the mean values and σ the standard deviation.

789
790
791



793

794 | Figure 8. Frequency distribution of *SPM* across the CoASTS and BioMaP marine regions. N795 | indicates the number of stations, *m* the mean values and σ the standard deviation.



798 Figure 9. Scatter plot $b_{bp}(488)/b_p(488)$ and $Chla$ for the diverse CoASTS and BioMaP marine
799 regions. N indicates the number of samples.

800

801 Table 9. Mean values of the $Chla$ specific absorption coefficient a_{ph}^* at 443 nm.

802

Region	$a_{ph}^*(443)$ [m^2mg^{-1}]
EMED (N=210)	<u>0.090±0.029</u>
WMED (N=190)	0.083±0.018
IBSH (N=129)	0.062±0.050
GRLS (N=54)	0.063±0.018
LIGS (N=121)	0.065±0.021
ADRS (N=119)	0.053±0.034
AAOT (N=613)	0.052±0.022
BLKS (N=695)	0.084±0.046
NORS (N=101)	0.061±0.108
BLTS (N=272)	0.047±0.014

803

804

805 Table 9 provides the mean specific absorption coefficients $a_{ph}^*(443)$ determined by the ratio of
806 $a_{ph}^*(443)/Chla$ across the various CoASTS and BioMaP marine regions. These mean values of
807 $a_{ph}^*(443)$ vary from 0.047 m^2mg^{-1} in the Baltic Sea (BLT) to 0.090 m^2mg^{-1} in the Eastern
808 Mediterranean Sea. It is warned that these latter values could be challenged by increased relative
809 uncertainties in the determination of both $a_{ph}^*(443)$ and $Chla$.

810

811

812 6. Summary and conclusions

813 The CoASTS and BiOMaP measurement programs led by the JRC Marine Optical
814 Laboratory benefitting of the collaboration of a number of European institutions and various
815 funding programs, were conceived to support satellite ocean color applications. Between 1995
816 and 2022, the two programs produced time-series at the AAOT site in the northern Adriatic Sea
817 and geographically distributed bio-optical measurements across the major European Seas. The
818 measurements delivered by the two programs beyond December 1998 include identical
819 quantities and are characterized by standardization of measurement methods, instruments, data
820 processing and quality assurance/control schemes.

821 This work introduces the CoASTS-BiOMaP data set comprising the near surface data
822 products from the CoASTS and BiOMaP measurement programs of major relevance for satellite
823 ocean color validation activities and bio-optical modelling.

824

825 7. Author contributions

826 Both authors, Giuseppe Zibordi and Jean-François Berthon, who implemented and co-led the
827 CoASTS and BiOMaP programs, contributed to the generation of the data set and to the writing
828 of the manuscript. Giuseppe Zibordi was a JRC Scientific Officer since the conception and up to
829 the end of the CoASTS and BiOMaP programs.

830

831 8. Competing interests

832 Both authors declare no competing interest.

833
834
835
836
837
838
839
840
841
842
843
844
845
846
847
848
849
850
851
852
853
854
855
856
857
858
859
860
861
862
863
864
865
866
867
868
869
870
871
872
873
874
875
876

9. Data availability

Interested researchers can download the CoASTS-BiOMaP data set at <https://doi.pangaea.de/10.1594/PANGAEA.971945> (Zibordi and Berthon, 2024). The original field measurements leading to the creation of this data set are currently not publicly available. However, ~~by endorsing the EU Policy Goals and the JRC Open Data principles (A. Friis-Christensen, J. P. Triaille, *JRC Data Policy*, EUR 27163 EN, Publications Office of the European Union, Luxembourg, 2019, ISBN 978 92 76 08380 1, doi:10.2760/637912, JRC115832), these field measurements may~~ they can be obtained from the authors upon a reasonable request.

10. Acknowledgments

The technical contributions to field measurements and laboratory analysis of many JRC and international colleagues are fully acknowledged: Cristina Targa, Stefania Grossi, Dirk Van der Linde, Lukasz Jankowski, Lyudmila Kamburska, Davide D'Alimonte, Marco Talone, Pietro Sciuto, Ilaria Cazzaniga, Jean Verdebout, Elisabetta Canuti, Alessandro Marchetti, Violeta Slabakova, Natalia Slabakova, Carolina Sa', Simone Colella, Gianluca Volpe, Seppo Kaitala, Jukka Seppala, Aleksandra Mazur.

Finally, Jaime Pitarch and Mike Twardowski are acknowledged for their outstanding reviews and constructive comments.

11. Funding support

Direct or indirect (through ship time) support to CoASTS and BiOMaP activities was provided by: the JRC through the EOSS and COLORS institutional projects, the European Union through the MAST-III, EUROFLEETS and JERICO programs, the North Atlantic Treaty Organization (NATO) through the Science for Peace Program, the US National Aeronautics and Space Administration (NASA), the European Space Agency (ESA), the Romanian Space Agency (ROSA), the Institute of Oceanology of the Bulgarian Academy of Sciences, the Institute of Oceanology of the Polish Academy of Sciences, the Finnish Environment Institute, the Italian National Research Council, the Portuguese Hydrographic Institute, the Italian Hydrographic Institute, the Royal Belgian Institute of Natural Sciences, the Hellenic Centre for Marine Research, the Université du Littoral Côte d' Opale.

The contribution of Giuseppe Zibordi to the finalization of this work was supported by the National Aeronautics and Space Administration through the GESTAR-II program under award number 80NSSC22M0001, while the contribution of Jean-François Berthon was supported by DG DEFIS (the European Commission Directorate-General for Defence Industry and Space) and the Copernicus Programme.

12. References

Belward, A., J. Hartstra, B. Baruth, P. Beck, C. Carmona Moreno, P. Churchill, M. Craglia, R. Crandon, D. Ehrlich, H. Eva, J. Fortuny Guasch, K.T. K.T., T. Kemper, H. Kerdiles, H., O.

877 Leo, P. Loudjani, G. Maenhout, P. Milenov, M. Pesaresi, B. Pinty, G. Zibordi, and J. Kreysa,
878 2022: A history of remote sensing at the JRC, Publications Office of the European Union,
879 Luxembourg, ISBN 978-92-76-49465-2, JRC127849.

880 Berthon, J. F., F. Mélin, and G. Zibordi, 2008: Ocean colour remote sensing of the optically
881 complex European seas. In *Remote sensing of the European seas* (pp. 35–52). Springer,
882 Dordrecht.

883 Berthon, J-F., G. Zibordi, J.P. Doyle, S. Grossi, D. van der Linde, and C. Targa, 2002: Coastal
884 Atmosphere and Sea Time Series (CoASTS), Part 2: Data Analysis. *NASA Tech. Memo.*
885 *2002–206892, Vol. 20*, S.B. Hooker and E.R. Firestone, Eds., NASA Goddard Space Flight
886 Center, Greenbelt, Maryland, 25 pp.

887 [Boss, E., W. H. Slade, M. Behrenfeld, and G. Dall’Olmo, 2009: Acceptance angle effects on the
888 beam attenuation in the ocean. *Opt. Express*, **17**\(3\), 1535-1550.](#)

889 [D’Alimonte, D., E.B. Shybanov, G. Zibordi, and T. Kajiyama, 2013: Regression of in-water
890 radiometric profile data. *Opt. Express*, **21**\(23\), 27707-27733.](#)

891 Doyle, J. P., and G. Zibordi, 2002: Optical propagation within a three-dimensional shadowed
892 atmosphere–ocean field: application to large deployment structures. *Appl. Opt.*, **41**(21), 4283–
893 4306.

894 Doyle, J.P., S.B. Hooker, G. Zibordi, and D. van der Linde, 2003: Validation of an In-Water,
895 Tower-Shading Correction Scheme. *NASA Tech. Memo. 2003–206892, Vol. 25*, S.B. Hooker
896 and E.R. Firestone, Eds., NASA Goddard Space Flight Center, Greenbelt, Maryland, 32 pp.

897 Ferrari, G. M., M. D. Dowell, S. Grossi, and C. Targa, 1996: Relationship between the optical
898 properties of chromophoric dissolved organic matter and total concentration of dissolved
899 organic carbon in the southern Baltic Sea region. *Mar. Chem.*, **55**(3–4), 299–316.

900 Ferrari, G. M., and S. Tassan, 1999: A method using chemical oxidation to remove light
901 absorption by phytoplankton pigments. *J. Phycolgy*, **35**(5), 1090–1098.

902 Gergely, M., and G. Zibordi, 2013: Assessment of AERONET-OC Lwn
903 uncertainties. *Metrologia*, **51**(1), 40.

904 Harris, R. L., 1999: *Information graphics: A comprehensive illustrated reference*. Oxford
905 University Press, USA, 448 pp.

906 Hooker S. B., C. S. Thomas, L. Van Heukelem, M. E. Russ, J. Ras, H. Claustre, L. Clementson,
907 E. Canuti, J.-F. Berthon, J. Perl, and C. Normandeau, 2010: The fourth SeaWiFS HPLC
908 analysis round-Robin experiment (SeaHARRE-4). NASA. Technical Memorandum –2010–
909 215857. NASA Goddard Space Flight Center, Greenbelt, Maryland, 75 pp.

910 IOCCG, 2000: Remote Sensing of Ocean Colour in Coastal, and Other Optically-Complex,
911 Waters. Sathyendranath, S. (ed.), *Reports of the International Ocean-Colour Coordinating*
912 *Group*, No. 3, IOCCG, Dartmouth, Canada.

913 IOCCG, 2019: IOCCG Ocean optics and biogeochemistry protocols for satellite ocean colour
914 sensor validation. *IOCCG Protocols Series*, No.3, IOCCG, Dartmouth, Canada.

915 Jeffrey, S.W., R.F.C. Mantoura, and S.W. Wright (Eds.), 1997: *Phytoplankton Pigments in*
916 *Oceanography: Guidelines to Modern Methods*. UNESCO Publishing, Paris, 661 pp.

917 Maffione, R. A., and D. R. Dana, 1997: Instruments and methods for measuring the backward-
918 scattering coefficient of ocean waters. *Appl. Opt.*, **36**(24), 6057–6067.

919 Morel, A., 1974: Optical properties of pure water and pure seawater. *Optical Aspects of*
920 [Oceanography](#).

921 [Morel, A., and Y.-H. Ahn, 1990: Optical efficiency factors of free-living marine bacteria:](#)
922 [Influence of bacterioplankton upon the optical properties and particulate organic carbon in](#)
923 [oceanic waters, *J. Mar. Res.*, **48**, 145–175.](#)

924 Morel, A., D. Antoine, and B. Gentili, 2002: Bidirectional reflectance of oceanic waters:
925 accounting for Raman emission and varying particle scattering phase function. *Appl.*
926 *Opt.*, **41**(30), 6289–6306.

927 Mueller, J. L., and R. W. Austin, 1995: Ocean Optics Protocols for SeaWiFS Validation,
928 Revision 1. *NASA Tech. Memo. 104566, Vol. 25*, S.B. Hooker and E.R. Firestone, Eds.,
929 NASA Goddard Space Flight Center, Greenbelt, Maryland, 67 pp.

930 Pérez, G. L., M. Galí, S. J. Royer, H. Sarmiento, J. M. Gasol, C. Marrasé, and R. Simó, 2016:
931 Bio-optical characterization of offshore NW Mediterranean waters: CDOM contribution to
932 the absorption budget and diffuse attenuation of downwelling irradiance. *Deep Sea Res. Part I*
933 *Oceanogr.*, **114**, 111–127.

934 [Smith, R. C., and K. S. Baker, 1981: Optical properties of the clearest natural waters \(200–800](#)
935 [nm\). *Appl. Opt.*, **20**\(2\), 177–184.](#)

936 [Stockley, N. D., R. Röttgers, D. McKee, I. Lefering, J. M. Sullivan, and M. S. Twardowski,](#)
937 [2017: Assessing uncertainties in scattering correction algorithms for reflective tube absorption](#)
938 [measurements made with a WET Labs AC-9. *Opt. Express*, **25**\(24\), A1139–A1153.](#)

939 Stramski, D., and D. A. Kiefer, 1991: Light scattering by microorganisms in the open
940 ocean. *Progr. Oceanogr.*, **28**(4), 343–383.

941 Strickland, J.D.H., and T.R. Parsons, 1972: A practical handbook of sea water analysis. *Fish.*
942 *Res. Board. Canada*, 310 pp.

943 Tassan, S., and G. M. Ferrari, 1995: An alternative approach to absorption measurements of
944 aquatic particles retained on filters. *Limnol. Oceanogr.*, **40**(8), 1358–1368.

945 Tassan, S., G. M. Ferrari, A. Bricaud, and M. Babin, 2000: Variability of the amplification factor
946 of light absorption by filter-retained aquatic particles in the coastal environment. *J. Plankton*
947 *Res.*, **22**(4), 659–668.

948 Thuillier, G., M. Hersé, T. Foujols, W. Peetermans, D. Gillotay, P. C. Simon, and H. Mandel,
949 2003: The solar spectral irradiance from 200 to 2400 nm as measured by the SOLSPEC
950 spectrometer from the ATLAS and EURECA missions. *Sol. Phys.*, **214**(1), 1–22.

951 [Twardowski, M. S., H. Claustre, S. A. Freeman, D. Stramski, and Y. Huot, 2007: Optical](#)
952 [backscattering properties of the "clearest" natural waters. *Biogeosciences*, **4**\(6\), 1041–1058.](#)

953 Twardowski, M. S., E. Boss, J. B. Macdonald, W. S. Pegau, A. H. Barnard, and J. R. V.
954 Zaneveld, 2001: A model for estimating bulk refractive index from the optical backscattering
955 ratio and the implications for understanding particle composition in case I and case II
956 waters. *J. Geophys. Res. Oceans*, **106**(C7), 14129–14142.

957 [Valente, A. and coauthors, 2016: A compilation of global bio-optical in situ data for ocean-](#)
958 [colour satellite applications. *Earth Syst. Sci. Data*, **8**\(1\), 235–252.](#)

959 Van der Linde, D., 1998: Protocol for total suspended matter estimate. *JRC Technical Note I-98-*
960 *182*, Joint Research Centre of the European Commission, Ispra, Italy, 15 pp.

961 Van Heukelem, L., and C. S. Thomas, 2001: Computer-assisted high-performance liquid
962 chromatography method development with applications to the isolation and analysis of
963 phytoplankton pigments. *J. Chromatogr. A*, **910**(1), 31–49.

964 [Voss, K. J., and S. Flora, 2017: Spectral dependence of the seawater–air radiance transmission](#)
965 [coefficient. *J. Atmos. Ocean. Technology*, **34**\(6\), 1203–1205.](#)

966 Werdell, P. J., and S. W. Bailey, 2005: An improved in-situ bio-optical data set for ocean color
967 algorithm development and satellite data product validation. *Remote Sens. Environ.*, **98**(1),
968 122–140.

969 Wet Labs, 2006: AC meter Protocol. WET Labs, Inc. Philomath, Oregon, 75 pp.
970 <https://miscslab.umeoce.maine.edu/ftp/classes/OO2015/Instruments/ac9acs/acprotocol.pdf>.

971 Whitmire, A. L., E. Boss, T. J. Cowles, and W. S. Pegau, 2007: Spectral variability of the
972 particulate backscattering ratio. *Opt. Express*, **15**(11), 7019–7031.

973 World Meteorological Organization, 1983: *Guide to the Meteorological Instruments and*
974 *Methods of Observation*, WMO–N.8, 517 pp.

975 Zaneveld, J. R. V., J. C. Kitchen, A. Bricaud, and C. C. Moore, 1992: Analysis of in-situ
976 spectral absorption meter data. In *Ocean Optics XI Proc. Soc. Photo-Optical Instrum. Eng.*
977 *(SPIE)*, 1750, 187–200.

978 Zhang, X., D. Stramski, R. A. Reynolds, and E. R. Blocker, 2019: Light scattering by pure water
979 and seawater: the depolarization ratio and its variation with salinity. *Appl. Opt.*, **58**(4), 991–
980 1004.

981 Zhang, X., L. Hu, and M. X. He, 2009: Scattering by pure seawater: Effect of salinity. *Opt.*
982 *Express*, 17(7), 5698–5710.

983 Zibordi, G., 2006: Immersion factor of in-water radiance sensors: assessment for a class of
984 radiometers. *J. Atmos. Ocean. Technology*, **23**(2), 302–313.

985 Zibordi, G., and J.-F. Berthon, 2024: Coastal Atmosphere & Sea Time Series (CoASTS) and the
986 Bio-Optical mapping of Marine optical Properties (BiOMaP): the near-surface marine bio-
987 optical data set. Accessible at: <https://doi.pangaea.de/10.1594/PANGAEA.968716>.

988 Zibordi, G., J.-F. Berthon, J.P. Doyle, S. Grossi, D. van der Linde, C. Targa, and L. Alberotanza,
989 2002: Coastal Atmosphere and Sea Time Series (CoASTS), Part 1: A Tower-Based Long-
990 Term Measurement Program. *NASA Tech. Memo. 2002–206892, Vol. 19*, S.B. Hooker and
991 E.R. Firestone, Eds., NASA Goddard Space Flight Center, Greenbelt, Maryland, 29 pp.

992 Zibordi, G., J.-F. Berthon, F. Mélin, and D. D'Alimonte, 2011: Cross-site consistent in situ
993 measurements for satellite ocean color applications: The BiOMaP radiometric dataset. *Remote*
994 *Sens. Environ.*, **115**(8), 2104–2115.

995 Zibordi, G., and B. Bulgarelli, 2007: Effects of cosine error in irradiance measurements from
996 field ocean color radiometers. *Appl. Opt.*, **46**(22), 5529–5538.

997 Zibordi, G., J. P. Doyle, and S. B. Hooker, 1999: Offshore tower shading effects on in-water
998 optical measurements. *J. Atmos. Ocean. Technology*, **16**(11), 1767–1779.

999 Zibordi, G., B. N. Holben, M. Talone, D. D'Alimonte, I. Slutsker, D. M. Giles, and M. G.
1000 Sorokin, 2021: Advances in the ocean color component of the aerosol robotic network
1001 (AERONET-OC). *J. Atmos. Ocean. Technology*, **38**(4), 725–746.

1002 Zibordi, G., S. B. Hooker, J. Mueller, and G. Lazin, 2004: Characterization of the immersion
1003 factor for a series of in-water optical radiometers. *J. Atmos. Ocean. Technology*, **21**(3), 501–
1004 514.

1005 Zibordi, G., and K. J. Voss, 2010: Field radiometry and ocean color remote sensing.
1006 In *Oceanography from Space* (pp. 307–334). Springer, Dordrecht.

1007

1008 **Appendix A: Acronyms**

1009	<u>AAOT</u>	<u>Acqua Alta Oceanographic Tower</u>
1010	<u>ADRS</u>	<u>Adriatic Sea</u>
1011	AERONET-OC	Ocean Color component of the Aerosol Robotic Network
1012	BiOMaP	Bio-Optical mapping of Marine Properties
1013	<u>BLKS</u>	<u>Black Sea</u>
1014	<u>BLTS</u>	<u>Baltic Sea</u>
1015	CDOM	Colored Dissolved Organic Matter
1016	CoASTS	Coastal-Atmosphere and Sea Time-Series
1017	<u>CTD</u>	<u>Conductivity, temperature and depth</u>
1018	<u>EMED</u>	<u>Eastern Mediterranean Sea</u>
1019	<u>GRLS</u>	<u>Greenland Sea</u>
1020	HPLC	High-Pressure Liquid Chromatography
1021	<u>IBS</u>	<u>Iberian Shelf</u>
1022	<u>LIGS</u>	<u>Ligurian Sea</u>
1023	JRC	Joint Research Center
1024	NASA	National Aeronautics and Space Administration
1025	NIST	National Institute of Standards and Technology
1026	<u>NORS</u>	<u>North Sea</u>
1027	NPL	National Physical Laboratory
1028	SeaWiFS	Sea-viewing Wide Field-of-view Sensor
1029	<u>WMED</u>	<u>Western Mediterranean Sea</u>
1030	WiSPER	Wire-Stabilized Profiling Environmental Radiometer
1031		